Analytical Performance Assessment of THz Wireless Systems

ALEXANDROS-APOSTOLOS A. BOULOGEORGOS[ID], **(Member, IEEE),**
EVANGELOS N. PAPASOTIRIOU, AND ANGELIKI ALEXIOU, (Member, IEEE)
Department of Digital Systems, University of Piraeus, 18534 Piraeus, Greece

Corresponding author: Alexandros-Apostolos A. Boulogeorgos (al.boulogeorgos@ieee.org)

ABSTRACT This paper is focused on providing the analytical framework for the quantification and evaluation of the joint effect of misalignment fading and hardware imperfections in the presence of multipath fading at terahertz (THz) wireless fiber extenders. In this context, we present the appropriate system model that incorporates the different operation, design, and environmental parameters. In more detail, it takes into account the transceivers antenna gains, the operation frequency, the distance between the transmitter (TX) and the receiver (RX), the environmental conditions, i.e., temperature, humidity, and pressure, the spatial jitter between the TX and RX antennas that results to antennas misalignment, the level of transceivers' hardware imperfections, and the stochastic characteristics of the wireless channel. Based on this model, we analyze and quantify the joint impact of misalignment and multipath fading by providing novel closed-form expressions for the probability and cumulative density functions of the composite channel. Moreover, we derive exact closed-form expressions for the outage probability for both cases of ideal and non-ideal radio frequency (RF) front-end. In addition, in order to quantify the detrimental effect of misalignment fading, we analytically obtain the outage probability in the absence of misalignment cases for both cases of ideal and non-ideal RF front-end. In addition, we extract the novel closed-form expressions for the ergodic capacity for the case of the ideal RF front-end and tight upper bounds for both the cases of ideal and non-ideal RF front-end. Finally, an insightful ergodic capacity ceiling for the non-ideal RF front-end case is provided.

INDEX TERMS Beyond 5G systems, ergodic capacity, fiber extender, hardware impairments, high frequency communications, misalignment fading, outage probability, performance analysis, terahertz communications, theoretical framework, α-μ fading.

I. INTRODUCTION

Over the last years, the proliferation of wireless devices and the increasing number of bandwidth-consuming internet services have significantly raised the demand for high data-rate transmission with very low latency. While the wireless world moves towards the fifth generation (5G), several technological advances, such as high order modulation schemes, massive multiple-input multiple-output systems and full duplexing, have been presented as promising enablers [1]. However, there is a lack of efficiency and flexibility in handling the huge amount of quality of service and experience oriented data [2], [3]. These realizations have motivated the exploitation of higher frequency bands, such as the terraherz (THz) band [4]–[7].

Despite the fact that THz band communications can offer an unprecented increase in the bandwidth and support ultra high data rates, yet they suffer from severe path attenuations,

transceivers antenna misalignment as well as hardware imperfections [8]. The path attenuation originates from the high frequencies of this band, which cause interaction and energy absorption by the molecules of the propagation medium [9]. As a result, a great amount of effort was put in modeling the THz channel particularities [10], evaluating their impact on the system's performance [11], [12] and proposing countermeasures [13]–[18]. On the other hand, antenna misalignment is caused due to the use of high directive antennas, which cannot be easily fully-aligned [19]. Finally, the hardware imperfections are the result of components mismatch and manufacturing defects in the radio frequency (RF) transceiver chain [20].

A. RELATED WORK
In general, the THz channel particularities were investigated in several works (see for example [11], [21]–[29] and

references therein). In more detail, Jornet and Akyildiz [21] presented a novel propagation model for electromagnetic nanoscale communications in the THz band, based on radiative transfer theory, whereas, in [11], the model was extended in order to incorporate the effect of molecular relaxation. Similarly, Yang *et al.* [22] provided an electromagnetic channel model for the body-centric nano-networks operating in the THz band. Additionally, in [23], a simplified path-loss model for the 275 − 400 GHz band was introduced, which was employed in [24] in order to evaluate the THz link performance in terms of average signal-to-noise ratio (SNR) and capacity. Furthermore, in [25], a multi-ray THz propagation model was presented, while Afsharinejad *et al.* [26] reported a path-loss model for nano-sensor networks operating in the THz band for plant foliage applications. Meanwhile, in [27], a propagation model for intra-body nano-scale communications was provided. Likewise, in [28], a path-loss model, which quantifies the total absorption loss assuming that air, natural gas and/or water are the components of the propagation medium, was discussed, whereas, in [29], a multi-ray THz propagation model was presented.

Although, all the above mentioned contributions revealed the particularities of the THz medium, they neglected the impact of fading, which can be generated due to scattering on aerosols in the atmosphere [30]. On the contrary, in Ekti *et al.* [31], Priebe *et al.* [32], Kim and Zajić [33], [34], Priebe *et al.* [35], and Afsharinejad *et al.* [36] presented suitable stochastic models that are able to accommodate the multipath fading effect in the THz band. In particular, Ekti *et al.* [31] introduced a multi-path THz channel model, where the attenuation factor was modeled as a Rayleigh or Nakagami-*m* distributions under the non-line-of-sight condition and as a Rician or Nakagami-*m* distribution under the line-of-sight (LoS) condition. Note that they supported their claim through experimental results. Meanwhile, Priebe *et al.* [32] conducted experiments and verified the existence of the shadowing effect in the 300 GHz band. Moreover, in [33] and [34], a two dimensional geometrical propagation model for indoor THz communications was proposed. Based on this model, they developed a parametric reference model for a THz multi-path Rician fading channel. Likewise, in [35], the influence of antenna directivities on the THz indoor channels for various antenna types was investigated, assuming Rician fading, whereas Afsharinejad *et al.* [36] used a log-distance shadowing path-loss model for THz nano-sensor networks communications in the vicinity of a plant.

The impact of transmitter (TX) and receiver (RX) beams misalignment was discussed in several published works, including [31], [35], [37], and [38]. However, despite the small transceiver antenna beam-width, due to the use of high directive antennas in the THz band, there are only three papers, which analyze its influence in the THz link [31], [35], [37]. In more detail, Ekti *et al.* [31] and Han and Akyildiz [37] assumed deterministic models to incorporate the impact of antennas' misalignment, while, in [35], it was

considered a part of the shadowing effect. The disadvantages of these models are that they are unable to accommodate the stochastic characteristics of phenomenons like thermal expansion, dynamic wind loads and weak earthquakes, which result in the sway of high-rise buildings and cause vibrations of the transceivers antennas; hence, the effect of misalignment between the TX and RX [39].

From the implementation point of view, in the THz band, the direct conversion architecture is of much hype, due to its low-complexity and cost-effective configuration [40]–[44]. The con of this architecture is that it is very sensitive to hardware imperfections, such as in-phase and quadrature imbalance, phase noise and amplifier non-linearities [45], [46]. In general, the effect of hardware imperfections was quantified in several contributions (see for example [47]–[60] and references therein) and it was concluded that they can significantly constrain the system's performance. However, despite of their paramount importance on the performance of THz wireless systems, the detrimental effects of hardware imperfections have been overlooked in the vast majority of reported contributions. Only very recently, their impact was experimentally reported in [41] and [44]. Specifically, Kallfass *et al.* [44] estimated the impact of hardware imperfections in the 300 GHz band. Finally, Koenig *et al.* [41] highlighted their detrimental effect in THz wireless fiber extender systems. However, to the best of the authors knowledge, there is no analytical study on the effect of hardware imperfections in the THz band.

B. MOTIVATION, NOVELTY AND CONTRIBUTION

To sum up, since the used frequency spectrum for 5G has limited capacity, THz wireless systems became an attractive complementing technology to the less flexible and more expensive optical-fiber connections [6], [13], where they can act as countermeasures to the connectivity gaps that exist between the radio frequency (RF) access network and the fiber optic based backbone network [4], [41], [42], [61]. This application scenario can be employed in developing countries, where there might not be much of a fiber optic structure and hence to increase its reach and bandwidth to the last mile, without requiring a huge amount of economic resources to dig up the current brown-field.

To the best of the authors' knowledge, the joint effect of misalignment and RF hardware imperfections over fading channel in the THz band have not been addressed in the open literature. Motivated by the above, this work is devoted to provide the generalized theoretical framework for the evaluation and quantification of the performance of THz wireless fiber extenders. The technical contribution of this paper is outlined below:

- We establish an appropriate system and channel model for the THz wireless fiber extender system, which accommodates the different design parameters as well as their interaction. These parameters include the distance between the TX and the RX, the TX and RX antennas' gains, the degree of TX and RX misalignment, the level

of hardware imperfection at the transceivers RF front-end, and the transmission power.

- In order to analyze the stochastic behavior of the wireless THz channel, we derive novel closed-form expression for the probability density function (PDF) and cumulative density function (CDF) of the distribution that model the composite channel, which accommodates the effect of both the misalignment and the multipath fading. Note that the mutlipath fading is modeled as an $\alpha - \mu$ distribution, which is a general form for several well-known channel models for multipath fading, such as Rayleigh, Nakagami-*m*, Weibull, shadow, and composite fading [62], [63], that have been experimentally verified in the THz systems, whereas, for the elevation and horizontal displacement at the RX's plane independent and identical Gaussian distributions are assumed. This is a commonly used approach in high-directive systems that are employed as wireless fiber extenders. However, this is the first paper that provides closed-form expression for analyzing the stochastic behavior of the composite (multipath and misalignment fading) THz wireless channel. Additionally, we present closed-form expressions for the PDF and CDF of the channel for the special cases, in which Rayleigh, Nakagami-*m*, Weibul and Gamma distributions are used to model the multipath fading effect.

- Based on the new channel model, we provide exact closed-form expressions for the outage probability that quantifies the performance of the THz wireless fiber extender system and take into account the level of misalignment and hardware imperfection. Simplified expression for the insightful case in which the transceivers have ideal RF front-ends are also reported. As benchmarks, we present closed-form expressions for the quantification of outage probabilities in both cases of ideal and non-ideal RF front-end in the absence of misalignment fading.

- Additionally, we extract novel closed-form expressions for the ergodic capacity in the case of ideal RF front-end and tight upper bounds for both cases of ideal and non-ideal RF front-end.

- Finally, we present an insightful ergodic capacity high SNR ceiling, for the practical case of non-ideal RF front-end.

C. ORGANIZATION AND NOTATIONS

The remainder of this paper is organized as follows. Section II presents the ideal and non-ideal RF front-end system models as well as the wireless THz channel model. Section III is focused on deriving the distribution of the composite misalignment and multipath fading channel. Moreover, the performance analysis in terms of outage probability and ergodic capacity for both cases of ideal and non-ideal RF front-end is provided in Section IV. Finally, respective numerical results and discussions are provided in Section V, while closing remarks are highlighted in Section VI.

Notations: In this paper, we use lower case bold letters to denote vectors. The operators $\mathbb{E}[\cdot]$ and $|\cdot|$ respectively denote the statistical expectation and the absolute value, whereas $\exp(x)$ and $\log_2(x)$ stand for the exponential function and the logarithmic function with base 2. Additionally, the operator $\ln(x)$ refers to the natural logarithm of x, while, the operators $\sqrt{x}$ and $\lim_{x \to a}(f(x))$ return the square root of x and the limit of the function $f(x)$ as x tends to a. Likewise, the set of the complex numbers is represented by $\mathbb{C}$, while $CN(x, y)$ denotes a x-mean complex Gaussian process with variance y. Meanwhile, $\delta(\cdot)$ stands for the Dirac's function. The upper and lower incomplete Gamma functions [64, eqs. (8.350/2) and (8.350/3)] are respectively denoted by $\Gamma(\cdot, \cdot)$ and $\gamma(\cdot, \cdot)$, while the Gamma function is represented by $\Gamma(\cdot)$ [64, eq. (8.310)]. Finally, $_2F_1(\cdot, \cdot; \cdot; \cdot)$ and $G_{p,q}^{m,n}\left(x \left| \begin{matrix} a_1, a_2, \cdots, a_p \\ b_1, b_2, \cdots, b_q \end{matrix} \right.\right)$ respectively stand for the Gauss hypergeometric function [65, eq. (4.1.1)] and the Meijer's G-function [64, eq. (9.301)], whereas $H_{p,q}^{m,n}\left[z \left| \begin{matrix} (a_1, b_1), \cdots, (a_p, b_p) \\ (c_1, d_1), \cdots, (c_p, d_p) \end{matrix} \right.\right]$ is the Fox H-function [66, eq. (8.3.1/1)].

II. SYSTEM & CHANNEL MODEL

This section is focused on presenting the system and channel model under consideration. In particular, in Section II-A, the system model is provided, while, in Section II-B, the channel model is given.

A. SYSTEM MODEL

As illustrated in Fig. 1.a, we consider a wireless fiber extender, in which the wireless link is utilized in the THz band. In order to countermeasure the channel attenuation, we assume that both the TX and RX are equipped with highly directive antennas. Suppose that the information signal, $x \in \mathbb{C}$, is conveyed over a flat fading wireless channel $h \in \mathbb{C}^1$ with additive noise $n \in \mathbb{C}$, the baseband equivalent received signal can be expressed as

$$y_i = hx + n, \tag{1}$$

where h, x and n are statistically independent. Likewise, n is modeled as a complex zero-mean additive white Gaussian process with variance equals N_o.

Although, the received signal model presented in (1), accommodates the impact of the wireless channel and noise, it neglects the effect of physical radio-frequency (RF) transceivers impefections, namely in-phase and quadrature imbalance (IQI), phase noise (PHN), as well as amplifier non-linearities, which, in high data rate systems, is detrimental [3], [45]. These imperfections generate a mismatch between the intended signal x and what is actually emitted and distort the received signal during the reception processing. In particular, IQI causes mirror-interference, while local oscillator

---

[1]This channel can, for example, be one of the subcarriers in a multi-carrier system based on orthogonal frequency-division multiplexing (OFDM).
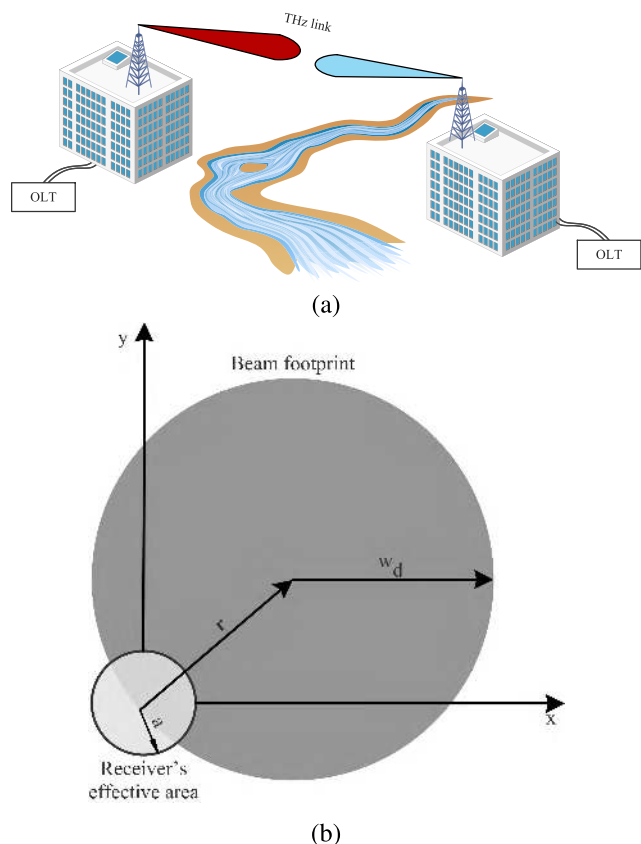
(a)

(b)

FIGURE 1. (a) System model under consideration. In this figure OLT stands for the optical line terminal. (b) RX's effective area and TX's beam footprint with misalignment on the RX's plane.

PHN results to adjacent carrier interference and amplifiers non-linearities to distributions that, according to Bussgant theorem, can be modeled as a complex Gaussian process [3]. Hence, in order to model their combined influence at a given flat fading subcarrier, we employ a generalized signal model [45], [67], which has been both theoretically and experimentally validated [68]–[71]. According to this model, the baseband equivalent received signal can be obtained as

$$y = h(x + n_t) + n_r + n. \qquad (2)$$

In (2), the parameters n_t and n_r are repsectively distortion noises from impairments in the TX and RX [67], and they can be defined as [67], [72]

$$n_t \sim CN(0, \kappa_t^2 P), \quad \text{and} \quad n_r \sim CN(0, \kappa_r^2 P|h|^2), \qquad (3)$$

where κ_t and κ_r are non negative design parameters that characterize the level of imperfections in the TX and RX hardware, respectively, while P stands for the average transmitted signal power. Finally, note that the κ_t and κ_r parameters are interpreted as the error vector magnitudes (EVMs) [73], [74], which is a common quality measure of RF transceivers and is the ratio of the average distortion magnitude to the average signal magnitude.

B. CHANNEL MODEL

The channel coefficient, h, can be obtained as

$$h = h_l h_p h_f, \qquad (4)$$

where h_l, h_p and h_f respectively model the path gain, the misalignment fading, which results in pointing errors, and the fading h_f.

1) PATH-GAIN COEFFICIENT
The path gain coefficient can be expressed as

$$h_l = h_{fl} h_{al}, \qquad (5)$$

where h_{fl} models the propagation gain and, according to Friis equation, can be modeled as [75]

$$h_{fl} = \frac{c\sqrt{G_t G_r}}{4\pi f d} \qquad (6)$$

where G_t and G_r respectively represent the antenna orientation dependent transmission and reception gains, c stands for the speed of light, f is the operating frequency and d is the distance between the TX and the RX. Additionally, h_{al} denotes the molecular absorption gain and can be evaluated as [23], [24]

$$h_{al} = \exp\left(-\frac{1}{2}\kappa_\alpha(f)d\right), \qquad (7)$$

where $\kappa_\alpha(f)$ denotes the absorption coefficient describing the relative area per unit of volume, in which the molecules of the medium are capable of absorbing the electromagnetic wave energy. Note that the main cause of absorption loss in millimeter and THz frequencies is the water vapor [11], [21], [24] that causes discrete, yet deterministic loss to the signals in the frequency domain. Other atmospheric molecules such as oxygen, also cause some level of loss to the signals, but it is minor when compared to the loss due to water vapor [24], [25]. The water vapor dominates the overall molecular absorption loss above 0.2 THz frequencies.

In order to evaluate the molecular absorption coefficient, the radiative transfer theory [76] as well the information provided by the high resolution transmission molecular absorption (HITRAN) database [77] are widely used. However, since THz fiber extenders are expected to operate in the $275 - 400$ GHz band, we utilize a simplified model for the molecular absorption loss in this band, which was initially presented in [23]. According to this model the absorption coefficient can be evaluated as

$$\kappa_\alpha(f) = y_1(f, v) + y_2(f, v) + g(f), \qquad (8)$$

where the parameters $y_1(f, v)$, $y_2(f, v)$ and $g(f)$ are defined as [24]

$$y_1(f, v) = \frac{A(v)}{B(v) + (\frac{f}{100c} - c_1)^2}, \qquad (9)$$

$$y_2(f, v) = \frac{C(v)}{D(v) + (\frac{f}{100c} - c_2)^2} \qquad (10)$$

and

$$g(f) = p_1 f^3 + p_2 f^2 + p_3 f + p_4 \tag{11}$$

where c stands for the speed of light and $c_1 = 10.835$ cm^{-1}, $c_2 = 12.664$ cm^{-1}, $p_1 = 5.54 \times 10^{-37}$ Hz^{-3}, $p_2 = -3.94 \times 10^{-25}$ Hz^{-2}, $p_3 = 9.06 \times 10^{-14}$ Hz^{-1}, $p_4 = -6.36 \times 10^{-3}$ and

$$A(v) = g_1 v (g_2 v + g_3), \tag{12}$$
$$B(v) = (g_4 v + g_5)^2, \tag{13}$$
$$C(v) = g_5 v (g_6 v + g_7), \tag{14}$$
$$D(v) = (g_8 v + g_9)^2 \tag{15}$$

with $g_1 = 0.2205$, $g_2 = 0.1303$, $g_3 = 0.0294$, $g_4 = 0.4093$, $g_5 = 0.0925$, $g_5 = 2.014$, $g_6 = 0.1702$, $g_7 = 0.0303$, $g_8 = 0.537$ and $g_9 = 0.0956$. Moreover, v stands for the volume mixing ratio of the water vapor (not to be confused with relative humidity) and can be evaluated as [23]–[25]

$$v = \frac{\phi}{100} \frac{p_w(T, p)}{p}, \tag{16}$$

where ϕ, p respectively stand for the relative humidity and the atmospheric pressure, while $p_w(T, p)$ is the saturated water vapor partial pressure in temperature T, and, according to Buck's equation [78], can be calculated as

$$p_w(T, p) = q_1 (q_2 + q_3 \phi_h) \exp\left(\frac{q_4 (T - q_5)}{T - q_6}\right), \tag{17}$$

with $q_1 = 6.1121$, $q_2 = 1.0007$, $q_3 = 3.46 \times 10^{-6}$ hPa^{-1}, $q_4 = 17.502$, $q_5 = 273.15\ ^o$K, $q_6 = 32.18\ ^o$K and ϕ_h being the pressure in hPa. Note that the model presented in (8) was shown to have great accuracy for up to 1 Km links in standard atmospheric conditions, i.e temperature of 296 ^{o}K, pressure of 101325 Pa and relative humidity of 0.5 [23].

2) MISALIGNMENT FADING COEFFICIENT

As illustrated in Fig. 1.b, we assume that the RX has a circular detection beam of radius α, covering an area A. Moreover, the TX has also a circular beam, which at distance d has a radius ρ, which belongs in the interval $0 \leq \rho \leq w_d$, where w_d is the maximum radius of the beam at distance d. Furthermore, both beams are considered on the positive $x - y$ plane and r is the pointing error expressed as the radial distance of the transmission and reception beams. Due to the symmetry of the beam shapes, h_p depends only on the radial distance $r = |r|$. Therefore, without loss of generality, it is assumed that the radial distance is located along the x axis. As a consequence and according to [79], the misalignment fading coefficient, h_p, which represents the fraction of the power collected by the RX, covering an area A at distance d can be approximated as

$$h_p(r; d) \approx A_o \exp\left(-\frac{2r^2}{w_{eq}^2}\right), \tag{18}$$

where w_{eq} is the equivalent beam-width, whereas A_o is the fraction of the collected power at $r = 0$ and can be calculated as

$$u = \frac{\sqrt{\pi} a}{\sqrt{2} w_d}, \tag{19}$$

with a being the radius of the RX effective area and w_d is the radius of the TX beam footprint at distance d. Moreover, note that the equivalent beam-width, w_{eq}^2, is related to w_d^2 through

$$w_{eq}^2 = w_d^2 \frac{\sqrt{\pi}\ \mathrm{erf}(u)}{2u \exp(-u^2)}. \tag{20}$$

By considering independent identical Gaussian distributions for the elevation and horizontal displacement [79], [80], the radial displacement at the RX follows a Rayleigh distribution with probability density function (PDF), which can be expressed as

$$f_r(r) = \frac{r}{\sigma_s^2} \exp\left(\frac{r^2}{2\sigma_s^2}\right), \tag{21}$$

where σ_s^2 is the variance of the pointing error displacement at the RX. By combining (18) and (21), the PDF of $|h_p|$ can be rewritten as [79]

$$f_{h_p}(x) = \frac{\gamma^2}{A_o^{\gamma^2}} x^{\gamma^2 - 1}, \quad 0 \leq x \leq A_o, \tag{22}$$

where

$$\gamma = \frac{w_{eq}}{2\sigma_s} \tag{23}$$

is the ratio between the equivalent beam width radius at the RX. Note that this model was extensively used in several studies in free space optical systems (see [81], [82] and references therein).

3) MULTIPATH FADING

In order to accomodate the multipath fading effect, we model $|h_f|$ as a generalized $\alpha - \mu$ distribution [83], with PDF that can be expressed as

$$f_{h_f}(x) = \frac{\alpha \mu^\mu}{\hat{h}_f^{\alpha \mu} \Gamma(\mu)} x^{\alpha \mu - 1} \exp\left(-\mu \frac{x^\alpha}{\hat{h}_f^\alpha}\right), \tag{24}$$

where $\alpha > 0$ is a fading parameter, μ is the normalized variance of the fading channel envelope, and $\hat{h}_f$ is the α-root mean value of the fading channel envelop. Note that this distribution is a general form for many well-known distributions, such as Rayleigh ($\alpha = 2$, $\mu = 1$), Nakagami-m ($\alpha = 2$ and μ is the fading parameter), Weibull ($\mu = 1$ and α is the fading parameter), etc. [84].

III. STATISTICAL ANALYSIS OF THE STOCHASTIC CHANNEL COEFFICIENT

The following theorems return the probability density function (PDF) and cumulative density function (CDF) of the

random process that is used to model the stochastic behavior of the channel, i.e.,

$$|h_{fp}| = |h_f||h_p|. \tag{25}$$

Theorem 1: The PDF of $|h_{fp}|$ can be analytically evaluated as

$$f_{|h_{fp}|}(x) = \gamma^2 A_0^{-\gamma^2} \frac{\mu^{\frac{\gamma^2}{\alpha}}}{\hat{h}_f^\alpha \Gamma(\mu)} x^{\gamma^2-1} \times \Gamma\left(\frac{\alpha\mu-\gamma^2}{\alpha}, \mu\frac{x^\alpha}{\hat{h}_f^\alpha} A_0^{-\alpha}\right). \tag{26}$$

Proof: Please see Appendix A. ∎

Theorem 2: The CDF of $|h_{fp}|$ can be obtained as

$$F_{|h_{fp}|}(x) = 1 - \frac{1}{\alpha} \frac{x^{\gamma^2}}{\hat{h}_f^{\gamma^2}} \frac{\gamma^2}{A_o^{\gamma^2}}$$
$$\times \sum_{k=0}^{\mu-1} \frac{\mu^{\frac{\gamma^2}{\alpha}}}{k!} \Gamma\left(\frac{\alpha k-\gamma^2}{\alpha}, \mu\frac{x^\alpha}{\hat{h}_f^\alpha} A_o^{-\alpha}\right). \tag{27}$$

Proof: Please see Appendix B. ∎

From (26) and (27), it is evident that the presented distribution depends on the multipath fading channels characteristics, which are modeled through the parameters α and μ, as well as the level of misalignment fading that is described via the parameters γ^2 and A_o.

A. SPECIAL CASE 1

In the special case in which the multipath fading can be modeled as a Rayleigh distribution, the PDF and CDF of $|h_{fp}|$ can be expressed, by setting $\alpha = 2$ and $\mu = 1$ in (26) and (27), as

$$f_{|h_{fp}|}^R(x) = \gamma^2 A_0^{-\gamma^2} \frac{1}{\hat{h}_f} x^{\gamma^2-1} \Gamma\left(\frac{2-\gamma^2}{2}, \frac{x^2}{\hat{h}_f} A_0^{-2}\right) \tag{28}$$

and

$$F_{|h_{fp}|}^R(x) = 1 - \frac{1}{2} \frac{x^{\gamma^2}}{\hat{h}_f^{\gamma^2}} \frac{\gamma^2}{A_o^{\gamma^2}} \Gamma\left(\frac{-\gamma^2}{2}, \frac{x^2}{\hat{h}_f^2} A_o^{-2}\right), \tag{29}$$

respectively.

B. SPECIAL CASE 2

In the special case in which the multipath fading can be modeled as a Nakagami-m distribution, the PDF and CDF of $|h_{fp}|$ can be expressed, by setting $\alpha = 2$ and $\mu = m$ in (26) and (27), as

$$f_{|h_{fp}|}^N(x) = \gamma^2 A_0^{-\gamma^2} \frac{m^{m-\frac{2m-\gamma^2}{2}}}{\hat{h}_f^2 \Gamma(m)} x^{\gamma^2-1}$$
$$\times \Gamma\left(\frac{2m-\gamma^2}{\alpha}, m\frac{x^2}{\hat{h}_f} A_0^{-2}\right) \tag{30}$$

and

$$F_{|h_{fp}|}^N(x) = 1 - \frac{1}{2} \frac{x^{\gamma^2}}{\hat{h}_f^{\gamma^2}} \frac{\gamma^2}{A_o^{\gamma^2}}$$
$$\times \sum_{k=0}^{m-1} \frac{m^{k+\frac{\gamma^2-2k}{2}}}{k!} \Gamma\left(\frac{2k-\gamma^2}{2}, m\frac{x^2}{\hat{h}_f^2} A_o^{-2}\right), \tag{31}$$

respectively.

C. SPECIAL CASE 3

In the special case in which the multipath fading can be modeled as a Weibull distribution, the PDF and CDF of $|h_{fp}|$ can be expressed, by setting $\mu = 1$ in (26) and (27), as

$$f_{|h_{fp}|}^W(x) = \gamma^2 A_0^{-\gamma^2} \frac{1}{\hat{h}_f^\alpha} x^{\gamma^2-1} \Gamma\left(\frac{\alpha-\gamma^2}{\alpha}, \frac{x^\alpha}{\hat{h}_f} A_0^{-\alpha}\right) \tag{32}$$

and

$$F_{|h_{fp}|}^W(x) = 1 - \frac{1}{\alpha} \frac{x^{\gamma^2}}{\hat{h}_f^{\gamma^2}} \frac{\gamma^2}{A_o^{\gamma^2}} \Gamma\left(\frac{-\gamma^2}{\alpha}, \frac{x^\alpha}{\hat{h}_f^\alpha} A_o^{-\alpha}\right), \tag{33}$$

respectively.

D. SPECIAL CASE 4

In the special case in which the THz wireless link suffers only from shadowing, then according to [63] and [85], $|h_f|$ can be modeled as a Gamma distribution, i.e., $\alpha = 1$, $\mu = m_s$ and $\widehat{h}_f = \Omega$. Hence, the CDF and the PDF of $|h_{fp}|$ can be respectively expressed as

$$f_{|h_{fp}|}^G(x) = \gamma^2 A_0^{-\gamma^2} \frac{m_s^{\gamma^2}}{\Omega \Gamma(m_s)} x^{\gamma^2-1} \times \Gamma\left(m_s - \gamma^2, \frac{m_s x}{\Omega A_0}\right) \tag{34}$$

and

$$F_{|h_{fp}|}^G(x) = 1 - \frac{x^{\gamma^2}}{\Omega^{\gamma^2}} \frac{\gamma^2}{A_o^{\gamma^2}}$$
$$\times \sum_{k=0}^{m_s-1} \frac{m_s^{\gamma^2}}{k!} \Gamma\left(k - \gamma^2, m_s \frac{x}{\Omega A_o}\right), \tag{35}$$

where Ω stands for the average power of shadowing in the area of interest and m_s is the shadowing severity such that as m_s increases the shadowing severity decreases. In the limit case in which $m_s \to \infty$, the distribution of $|h_f|$ tends to the Dirac's distribution as

$$f_{|h_f|}^\infty(x) = \delta(x - \Omega). \tag{36}$$

In other words, in the limit case, there is no shadowing effect.

IV. PERFORMANCE ANALYSIS

In this section, the instantaneous SNR and signal to noise plus distortion ratio (SNDR) are derived and accordingly the system's performance is quantified, in terms of outage probability and ergodic capacity. In more detail, in Section IV-A, the instantaneous SNR and SNDR for the cases of ideal and

non-ideal RF front-end are respectively provided, whereas, in Section IV-B novel closed-form expressions for the evaluation of the corresponding outage probabilities are given. Additionally, in Section IV-C, an exact closed-form expression and a simplified upper bound for the ergodic capacity in the case of ideal RF front-end as well as a tight upper bound and a ceiling for the ergodic capacity in the case of non-ideal RF front-end are extracted.

A. INSTANTENOUS SNR & SNDR

This section is focused on presenting the instantaneous SNR in the case of ideal RF front-end and the SNDR in the case of non-ideal RF front-end.

1) IDEAL RF FRONT-END

In the case of ideal RF front-end, based on (1), the instantaneous SNR of the received signal can be obtained as

$$\rho_i = \frac{|h|^2 P}{N_o}. \tag{37}$$

2) NON-IDEAL RF FRONT-END

The instantaneous SNDR can be expressed as

$$\rho = \frac{|h|^2 P}{\kappa^2 |h|^2 P + N_o}, \tag{38}$$

where $\kappa^2 = \kappa_t^2 + \kappa_r^2$.

B. OUTAGE PROBABILITY
1) IDEAL RF FRONT-END

In the case of ideal RF front-end, Proposition 1 provides a novel closed-form expression for the evaluation of the outage probability in the presence of misalignment fading, while Lemma 1 returns the corresponding expressions in the absence of misalignment fading.

Proposition 1: In the case of ideal RF front-end, the outage probability, in the presence of misalignment fading, can be analytically evaluated as

$$P_o^{\text{id}}(\gamma_{th}) = F_{|h_{fp}|}\left(\sqrt{\frac{\gamma_{th} N_o}{|h_l|^2 P}}\right), \tag{39}$$

where γ_{th} stands for the SNR threshold.

Proof: The outage probability can be defined as

$$P_o^{\text{id}}(\gamma_{th}) = P_r(\rho_i \leq \gamma_{th}), \tag{40}$$

which, based on (37), can be rewritten as

$$P_o^{\text{id}}(\gamma_{th}) = P_r\left(\frac{|h|^2 P}{N_o} \leq \gamma_{th}\right), \tag{41}$$

or, after some algebraic manipulations as

$$P_o^{\text{id}}(\gamma_{th}) = P_r\left(|h_{fp}| \leq \sqrt{\frac{\gamma_{th} N_o}{|h_l|^2 P}}\right), \tag{42}$$

which can be rewritten as (39). This concludes the proof. ∎

Lemma 1: In the case of ideal RF front-end, the outage probability, in the absence of misalignment fading, can be obtained as

$$P_o^{\text{id,wm}} = \frac{\gamma\left(\mu, \mu \frac{\gamma_{th}^{\frac{\alpha}{2}} N_o^{\frac{\alpha}{2}}}{|h_l|^\alpha \hat{h}_f^\alpha P^{\frac{\alpha}{2}}}\right)}{\Gamma(\mu)}. \tag{43}$$

Proof: Similar to (42), in the absence of misalignment fading, the outage probability can be expressed as

$$P_o(\gamma_{th}) = P_r\left(|h_f| \leq \sqrt{\frac{\gamma_{th} N_o}{|h_l|^2 P}}\right), \tag{44}$$

or equivalently

$$P_o(\gamma_{th}) = F_{|h_f|}\left(\sqrt{\frac{\gamma_{th} N_o}{|h_l|^2 P}}\right), \tag{45}$$

which, by using (66), can be rewritten as in (43). This concludes the proof. ∎

2) NON-IDEAL RF FRONT-END

In the case of non-ideal RF front-end, Proposition 2 provides a novel closed-form expression for the evaluation of the outage probability, whereas Lemma 2 returns the corresponding expressions in the absence of misalignment fading.

Proposition 2: The outage probability can be analytically evaluated as

$$P_o(\gamma_{th}) = \begin{cases} F_{|h_{fp}|}\left(\sqrt{\frac{\gamma_{th} N_o}{P|h_l|^2 (1 - \gamma_{th}\kappa^2)}}\right), & \text{for } \gamma_{th} \leq \frac{1}{\kappa^2} \\ 1, & \text{otherwise} \end{cases} \tag{46}$$

Proof: Please see Appendix C. ∎

Lemma 2: In the case of non-ideal RF front-end, the outage probability, in the absence of misalignment fading, can be obtained as

$$P_o^{\text{wm}} = \begin{cases} \dfrac{\gamma\left(\mu, \mu \frac{\gamma_{th}^{\frac{\alpha}{2}} N_o^{\frac{\alpha}{2}}}{|h_l|^\alpha \hat{h}_f^\alpha P^{\frac{\alpha}{2}} (1 - \gamma_{th}\kappa^2)^{\frac{\alpha}{2}}}\right)}{\Gamma(\mu)}, & \text{for } \gamma_{th} \leq \frac{1}{\kappa^2} \\ 1, & \text{otherwise} \end{cases} \tag{47}$$

Proof: Please see Appendix D. ∎

From (43) and (46), we observe that the outage probability is an increasing function of γ_{th}. Moreover, by comparing (39) with (46) and (43) with (47), it becomes evident that the maximum spectrum efficiency of the selected transmission scheme, which is an increasing function of γ_{th}, is limited by the level of hardware imperfections. In more detail, if a transmission scheme is selected that requires a SNR threshold that is higher than $\frac{1}{\kappa^2}$, then the system is always in an outage state.

$$C_{id} = \frac{\Xi \mathcal{P}^{-\frac{\mathcal{B}+1}{2}}}{2\ln(2)} H_{3,4}^{4,1}\left[\frac{L}{\mathcal{P}^{\frac{\alpha}{2}}}\left|\begin{array}{c}\left(-\frac{\mathcal{B}+1}{2},\frac{\alpha}{2}\right),\left(1-\frac{\mathcal{B}+1}{2},\frac{\alpha}{2}\right),(1,1)\\(0,1),(K,1),\left(-\frac{\mathcal{B}+1}{2},\frac{\alpha}{2}\right),\left(-\frac{\mathcal{B}+1}{2},\frac{\alpha}{2}\right)\end{array}\right.\right] \tag{48}$$

C. ERGODIC CAPACITY

1) IDEAL RF FRONT-END

In the case of ideal RF front-end, Theorem 3 returns a novel closed-form expression for the evaluation of the ergodic capacity, whereas Theorem 4 provides a simplified upper bound.

Theorem 3: The ergodic capacity can be analytically evaluated as in (48), given in the top of this page. In (48),

$$\mathcal{P} = \frac{|h_l|^2 P}{N_o}, \tag{49}$$

$$\mathcal{B} = \gamma^2 - 1, \tag{50}$$

$$K = \frac{\alpha\mu - \gamma^2}{\alpha}, \tag{51}$$

$$L = \frac{\mu}{\hat{h}_f^\alpha A_0^a} \tag{52}$$

and

$$\Xi = \gamma^2 A_0^{-\gamma^2} \frac{\mu^{\mu - \frac{\mu\alpha - \gamma^2}{\alpha}}}{\hat{h}_f^\alpha \Gamma(\mu)}. \tag{53}$$

Proof: Please see Appendix E. ∎

Theorem 4: The ergodic capacity can be upper bounded as

$$C_{id} \le \log_2\left(1 + \frac{P|h_l|^2}{N_o}\frac{\gamma^2 A_o^2}{2+\gamma^2}\frac{\hat{h}_f^2}{\mu^{\frac{2}{\alpha}}}\frac{\Gamma\left(\frac{2}{\alpha}+\mu\right)}{\Gamma(\mu)}\right). \tag{54}$$

Proof: Please see Appendix F. ∎

2) NON-IDEAL RF FRONT-END

In the case of non-ideal RF front-end, the following theorem returns an upper bound of the ergodic capacity.

Theorem 5: The ergodic capacity can be upper bounded as

$$C \le \log_2\left(1 + \frac{P|h_l|^2 \frac{\gamma^2 A_o^2}{2+\gamma^2}\frac{\hat{h}_f^2}{\mu^{\frac{2}{\alpha}}}\frac{\Gamma\left(\frac{2}{\alpha}+\mu\right)}{\Gamma(\mu)}}{\kappa^2 P|h_l|^2 \frac{\gamma^2 A_o^2}{2+\gamma^2}\frac{\hat{h}_f^2}{\mu^{\frac{2}{\alpha}}}\frac{\Gamma\left(\frac{2}{\alpha}+\mu\right)}{\Gamma(\mu)} + N_o}\right). \tag{55}$$

Proof: In the case of non-ideal RF front-end, the ergodic capacity can be defined as

$$C = \mathbb{E}\left[\log_2\left(1 + \frac{p}{\kappa^2 p + N_o}\right)\right], \tag{56}$$

where

$$p = |h|^2 P. \tag{57}$$

By applying Jensen's inequality [86] into (56), we can upper-bound the ergodic capacity as

$$C \le \log_2\left(1 + \frac{\mathbb{E}[p]}{\kappa^2 \mathbb{E}[p] + N_o}\right), \tag{58}$$

which, by employing (106) gives (55). This concludes the proof. ∎

The following lemma returns a capacity ceiling in the high SNR regime.

Lemma 3: As the SNR tends to infinity, the ergodic capacity is constrained by

$$C_c = \log_2\left(1 + \frac{1}{\kappa^2}\right). \tag{59}$$

Proof: The capacity ceiling can be defined as

$$C_c = \lim_{\tilde{\rho}\to\infty} C, \tag{60}$$

where $\tilde{\rho}$ represents the average SNR. Based on (55), (60) can be equivalently expressed as

$$C_c = \lim_{N_o\to 0}\left(\log_2\left(1 + \frac{P|h_l|^2 \frac{\gamma^2 A_o^2}{2+\gamma^2}\frac{\hat{h}_f^2}{\mu^{\frac{2}{\alpha}}}\frac{\Gamma\left(\frac{2}{\alpha}+\mu\right)}{\Gamma(\mu)}}{\kappa^2 P|h_l|^2 \frac{\gamma^2 A_o^2}{2+\gamma^2}\frac{\hat{h}_f^2}{\mu^{\frac{2}{\alpha}}}\frac{\Gamma\left(\frac{2}{\alpha}+\mu\right)}{\Gamma(\mu)} + N_o}\right)\right), \tag{61}$$

which, after some algebraic manipulations, can be rewritten as (59). This concludes the proof. ∎

From (59), it is evident that maximum achievable ergodic capacity is constrained by the transceivers level of hardware imperfections and not by the multipath and/or misalignment fading characteristics.

V. RESULTS AND DISCUSSION

In this section, we investigate the joint effects of the deterministic and stochastic path-gain, i.e., misalignment and multipath fading, components as well as the impact of transceivers hardware imperfections in the outage and ergodic capacity performance of the THz wireless fiber extender by illustrating analytical and simulation results. In particular, we consider the following insightful scenario. Unless otherwise is stated, it is assumed that $G_t = G_r = 55$ dBi,[2] $\alpha = 2$, and $\mu = 4$. Moreover, standard environmental conditions, i.e., $\phi = 50\%$, $p = 101325$ Pa, and $T = 296\ ^oK$, are assumed. Furthermore, we consider that the transmission distance ranges between 10 and 100 m. Finally, unless otherwise is stated, in all the illustrations, the solid curves represent analytical values obtained through the derived formulas, while the markers represent Monte-Carlo simulation results.

---

[2]According to [14], [41], and [87]–[89], this antenna gain can be practically achieved by employing high-gain Cassegrain antennas, which are widely used for wireless fiber extender appliances in the millimeter and THz bands.

A. IMPACT OF THE DETERMINISTIC PATH-GAIN

Fig. 2 depicts the outage probability as a function of the transmission distance, d, for different values of f and $\frac{P}{N_o}$, assuming ideal RF front-end and $\sigma_s = 0.01$ m. As expected, for fixed f and $\frac{P}{N_o}$, as d increases, the outage probability also increases. For instance, for $f = 275$ GHz and $\frac{P}{N_o} = 10$ dB, the outage probability increases for about 96%, as the distance alters from 10 to 15 m. This indicates that even relatively small changes in the transmission distance can result in significant alterations on the system's outage performance. Additionally, for a given d and $\frac{P}{N_o}$, we observe that as the frequency increases, the propagation loss increases, or equivalently the deterministic path-gain decreases; hence, the outage probability increases. Finally, for a fixed d and f, as $\frac{P}{N_o}$ increases, the outage probability decreases. For example, for $d = 15$ m and $f = 300$ GHz, by changing the $\frac{P}{N_o}$ from 10 to 25 dB, the outage probability is decreased from 1.66786×10^{-5} to 1.8633×10^{-11}.

FIGURE 3. Outage probability vs relative humidity and temperature, assuming ideal RF front-end, $f = 300$ GHz, $d = 10$ m and $\frac{P}{N_o} = 50$ dB, $\gamma_{th} = 0.5$, and $\sigma_s = 0.01$ m.
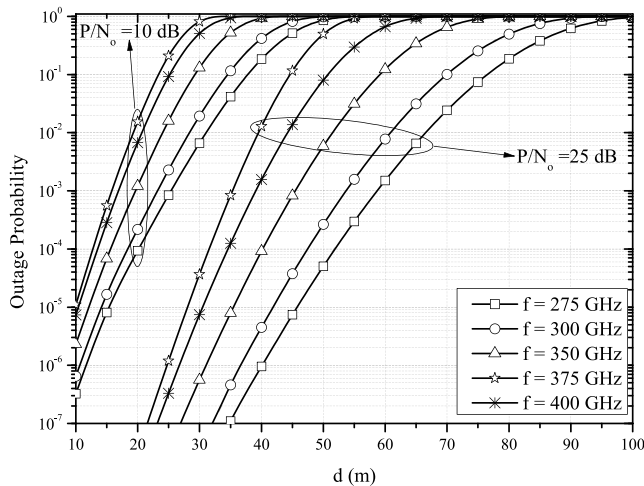
FIGURE 2. Outage probability vs transmission distance, for different values of f and normalized transmission power equals 10 and 25 dB.

Fig. 3 illustrates the impact of atmospheric conditions on the system's outage performance. In particular, the outage probability is plotted as a function of the relative humidity and the temperature, assuming ideal RF front-end, $f = 300$ GHz, $d = 10$ m and $\frac{P}{N_o} = 50$ dB, $\gamma_{th} = 0.5$, and $\sigma_s = 0.01$ m. From this figure, it is evident that, for a given relative humidity, as the temperature increases, the molecular absorption also increases; hence, the outage probability increases. For instance, for $\phi = 50\%$, a temperature alteration from 280 ^{o}K to 290 ^{o}K results in about 1.8% outage performance degradation. Moreover, we observe that for a fixed temperature, as the relative humidity increases, the outage probability also increases. For example, for $T = 280$ ^{o}K, when the relative humidity shifts from 50% to 60%, a 0.39% outage probability increase occurs. In other words, we observe that the temperature alteration can result to a slightly more significant effect on the system's outage performance compared to the humidity alteration. Moreover, these results reveal the
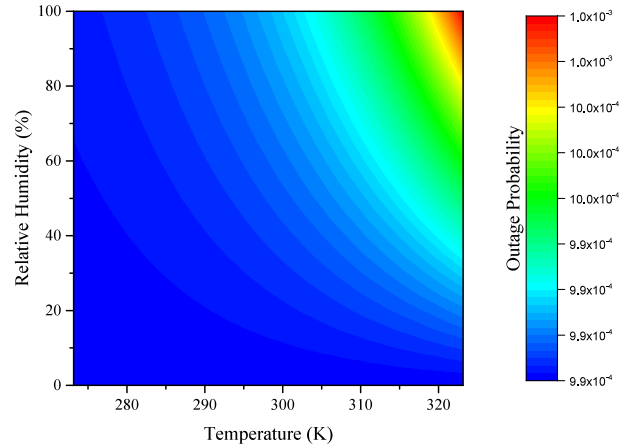
importance of taking into account the atmospheric conditions, when designing and establishing a THz wireless link.

Fig. 4 shows the ergodic capacity as a function of the transmission distance and the relative humidity, assuming ideal RF front-end, $f = 380$ GHz, $\frac{P}{N_o} = 25$ dB and $\sigma_s = 0.01$ m. As expected, for a fixed relative humidity, as the transmission distance increases, the deterministic path-loss increases; hence, the ergodic capacity decreases. Similarly, for a given transmission distance, as the relative humidity increases, the absorption loss also increases; therefore, the ergodic capacity decreases. Finally, we observe that the impact of propagation loss is more severe compared to the one of the molecular absorption loss, since the ergodic capacity degradation due to a transmission distance increase is much more severe than the corresponding degradation due to a relative humidity increase.
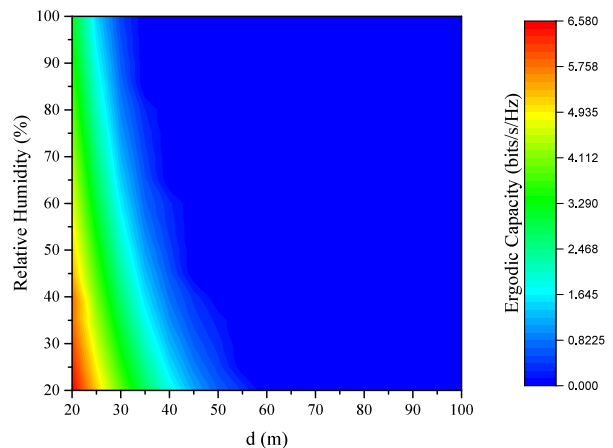
FIGURE 4. Capacity vs distance and relative humidity, assuming ideal RF front-end, $f = 380$ GHz, $\frac{P}{N_o} = 25$ dB, and $\sigma_s = 0.01$ m.

Fig. 5 depicts the ergodic capacity as a function of the frequency and the relative humidity, assuming ideal
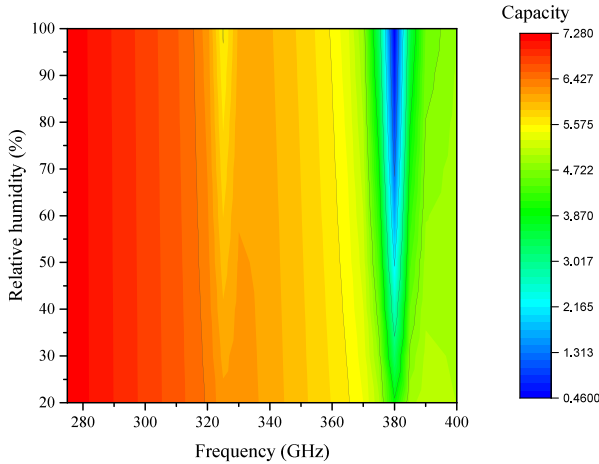
FIGURE 5. Capacity vs frequency and relative humidity, assuming ideal RF front-end, $d = 30$ m, $\frac{P}{N_o} = 25$ dB, and $\sigma_s = 0.01$ m.
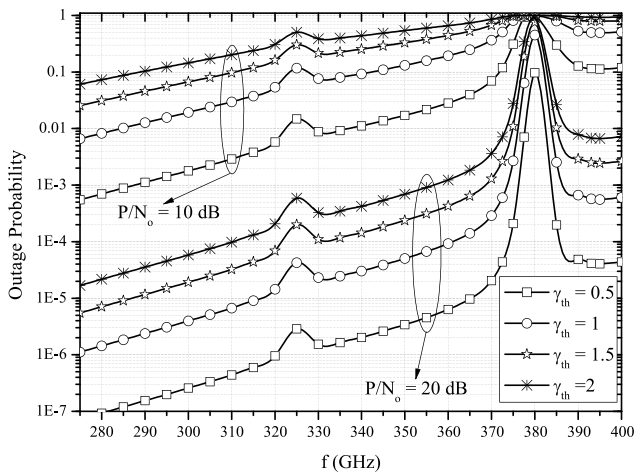

FIGURE 7. Outage probability vs $\frac{P|h_l|^2}{N_o}$ for different values of μ and γ_{th}, assuming ideal RF front-end and $d = 30$ m.

FIGURE 6. Outage probability vs the operation frequency for different values of γ_{th} and $\frac{P}{N_o}$, assuming ideal RF front-end and $d = 20$ m.

Fig. 6 demonstrates the outage probability as a function of the operation frequency for different values of γ_{th} and $\frac{P}{N_o}$, assuming ideal RF fron-end, $d = 20$ m and $\sigma_s = 0.01$ m. As expected, for a fixed frequency, as γ_{th} increases, the outage probability also increases. For instance, for $f = 380$ GHz and $\frac{P}{N_o} = 20$ dB, an 89.38% increase of the outage probability is observed, as the γ_{th} alters from 0.5 to 2. Moreover, this figure reveals the frequency dependency of the system's outage performance as well as that the worst operation frequency is 380 GHz.

B. IMPACT OF MULTIPATH FADING

In Fig. 7, the outage probability is depicted as a function of $\frac{P|h_l|^2}{N_o}$ for different values of μ and γ_{th}, assuming ideal RF front-end, $d = 30$ m and $\gamma^2 = 1$. As a benchmark, the worst case scenario of Rayleigh fading is plotted. From this figure, we observe that, for a given μ and γ_{th}, as $\frac{P|h_l|^2}{N_o}$ increases, the outage probability decreases. Moreover, for a given $\frac{P|h_l|^2}{N_o}$ and μ, as γ_{th} increases, the outage probability also increases. For instance, for $\frac{P|h_l|^2}{N_o} = 40$ dB and $\mu = 8$, the outage probability increases for about 287.4%, as γ_{th} alters from 1 to 15. Finally, for a fixed $\frac{P|h_l|^2}{N_o}$ and γ_{th}, as μ increases, i.e., as the strength of the LoS component increases, the system's outage behavior improves.

Fig. 8 shows the joint impact of multipath and misalignment fading on the ergodic capacity. Specifically, the ergodic capacity is plotted as a function of $\frac{P}{N_o}$ for different values of μ and σ_s, assuming ideal RF front-end and $d = 30$ m. Note that, in this figure, the numerical results are shown with continuous lines, while markers are employed to illustrate the simulation results. The analytical results coincide with the simulations, verifying the derived expressions. Moreover, the ergodic capacity for the special case in which the multipath fading follows Rayleigh distribution is plotted as a benchmark. This figure reveals that the impact of misalignment fading is somewhat more detrimental compared to the one of the

RF front-end, d=30 m, $\frac{P}{N_o} = 25$ dB and $\sigma_s = 0.01$ m. From this figure, it is evident that the impact of the level of humidity on the ergodic capacity depends on the operation frequency. In more detail, we observe that up to 320 GHz the effect of relative humidity alteration is relatively low, whereas in the 380 GHz region, it is detrimental. For example, in 300 GHz, a relative humidity alteration from 30% to 60% results to a 0.1% ergodic capacity degradation, whereas the same alteration in the 380 GHz causes a corresponding 98.9% decrease. Moreover, in the 400 GHz region, although the free space path loss is higher compared to the one in the 380 GHz region, the achievable ergodic capacity is much higher. This is the impact of the high molecular absorption in the 380 GHz, which is one of the water vapor resonance frequencies [23], [90]. These observations indicate the importance of taking into account the variation of the environmental conditions in a geographical area as well as the molecular absorption phenomenon, when selecting the operation frequency.
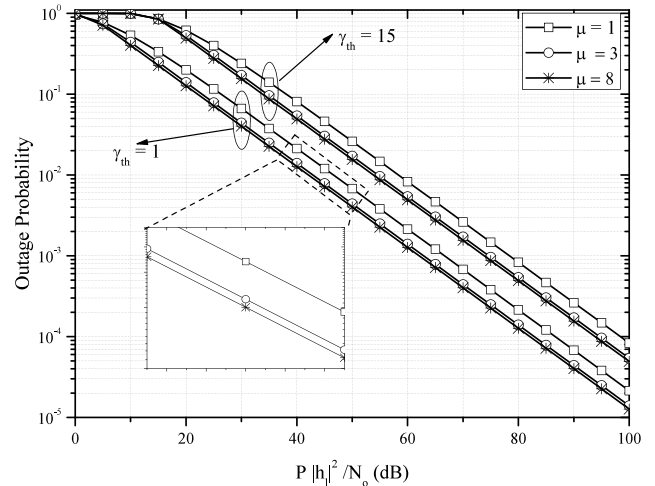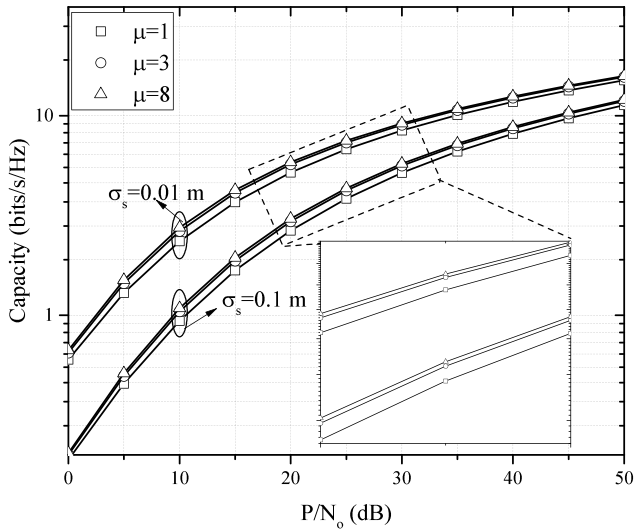
FIGURE 8. Capacity vs $\frac{P}{N_o}$ for different values of μ and σ_s, assuming ideal RF front-end, $\alpha = 2$ and $d = 30$ m.

multipath fading. Moreover, we observe that the increase of the transmission power can act as a countermeasure to the joint impact of multipath and misalignment fading in the ergodic capacity.

C. IMPACT OF MISALIGNMENT FADING

Fig. 9 illustrates the impact of misalignment fading on the system's outage performance. In more detail, the outage probability is provided as a function of the spatial jitter, σ_s, for different values of $\frac{P}{N_o}$, assuming ideal RF front-end, $d = 30$ m, $\gamma_{th} = 1$, $\alpha = 2$ and $\mu = 4$, for the cases in which the system suffers from misalignment fading (continuous lines) or not (dashed lines). As expected, for a given $\frac{P}{N_o}$, as σ_s increases, the outage probability also increases. For
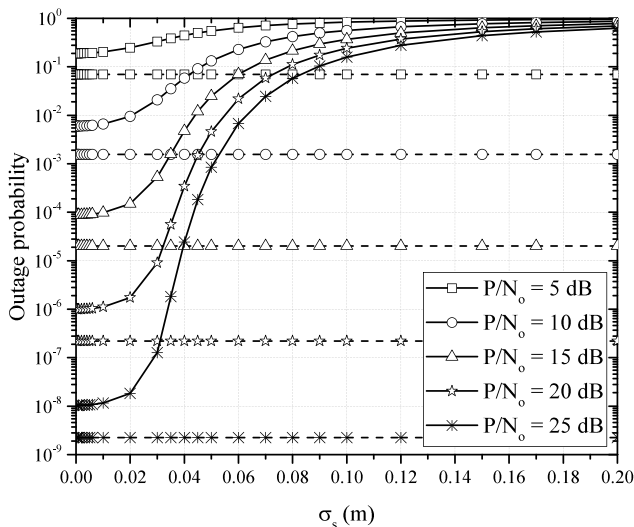

FIGURE 9. Outage probability vs σ_s for different values of $\frac{P}{N_o}$, assuming ideal RF front-end, $d = 30$ m, $\gamma_{th} = 1$, $\alpha = 2$ and $\mu = 4$, for the cases in which the system suffers from misalignment fading (continuous lines) or not (dashed lines).

example, for $\frac{P}{N_o} = 10$ dB, a σ_s alteration from 0.02 to 0.05 causes a 1298.1% outage performance degradation, whereas, for $\frac{P}{N_o} = 20$ dB, the same σ_s alteration results to a 264040% outage performance degradation. This indicates that the impact of misalignment increases as the $\frac{P}{N_o}$ increases.

Fig. 10 depicts the ergodic capacity versus σ_s for different values of $\frac{P}{N_o}$, assuming ideal RF front-end, $d = 30$ m, $\alpha = 2$ and $\mu = 4$. In this figure, the numerical results are shown with continuous lines, while markers are employed to illustrate the simulation results. It becomes evident from this figure that the analytical results are identical with simulation results; thus, verifying the presented analytical framework. Moreover, it is observed that the spatial jitter causes a significant ergodic capacity degradation. In more detail, we observe that, for a given $\frac{P}{N_o}$, as σ_s increases, the ergodic capacity decreases. Furthermore, for a given σ_s, as $\frac{P}{N_o}$ increases, the RX antenna is able to collect more of the emitted power; hence, the ergodic capacity also increases. For instance, for $\sigma_s = 0.05$, a $\frac{P}{N_o}$ increase from 10 to 20 dB results to a 134.63% ergodic capacity improvement.
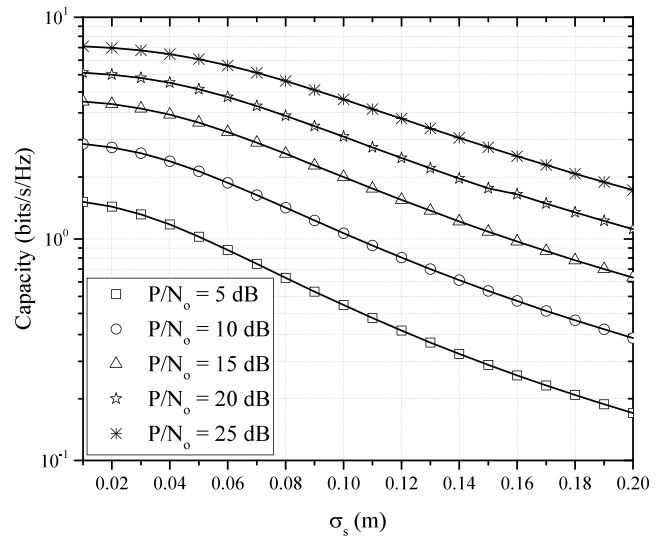

FIGURE 10. Capacity vs σ_s for different values of $\frac{P}{N_o}$, assuming ideal RF front-end, $d = 30$ m, $\alpha = 2$ and $\mu = 4$.

D. IMPACT OF HARDWARE IMPERFECTIONS

Fig. 11 illustrates the impact of hardware imperfections on the system's outage performance. Specifically, the outage probability is plotted as a function of $\frac{P|h_l|^2}{N_o}$ for different values of $\kappa_{tr} = \kappa_t = \kappa_r$ and γ_{th}, assuming $\alpha = 2$, $\mu = 4$ and $d = 20$ m. As a benchmark, the corresponding outage probability in the case of ideal RF front-end is depicted. From this figure, it is evident that, for a given $\frac{P|h_l|^2}{N_o}$ and γ_{th}, as the level of hardware imperfection increases, the outage probability also increases. Moreover, for a fixed $\frac{P|h_l|^2}{N_o}$, as γ_{th} increases, the impact of hardware imperfections become more severe. For example, for $\frac{P|h_l|^2}{N_o} = 30$ dB and $\gamma_{th} = 1$, the outage probability increases for about 9.3%, when κ_{tr} alters from 0.10 to 0.30, whereas, for the same $\frac{P|h_l|^2}{N_o}$ and κ_{tr} alteration,
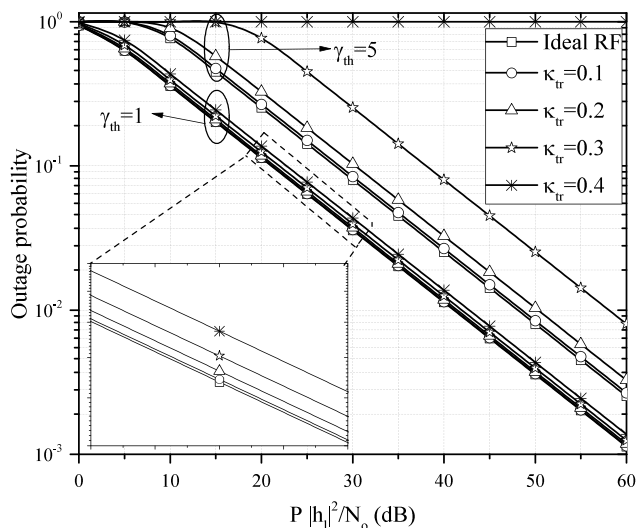
FIGURE 11. Outage probability vs $\frac{P|h_l|^2}{N_o}$ for different values of $\kappa_{tr} = \kappa_t = \kappa_r$ and γ_{th}, assuming $\alpha = 2$, $\mu = 4$ and $d = 20$ m.

the outage probability increases for about 200%, when $\gamma_{th} = 5$. This indicates that by using transmission schemes with lower spectral efficiency, we can significantly constrain the impact of hardware RF imperfections. Finally, in the worst case scenario in which $\kappa_{tr} = 0.4$ and $\gamma_{th} = 5$, the condition $\gamma_{th} \geq \frac{1}{\kappa^2}$ is satisfied, and the outage probability is always 1.

Fig. 12 demonstrates the joint effect of hardware imperfections and misalignment fading on the system's outage performance. In particular, the outage probability is given as a function of κ_{tr}, for different values of σ_s, assuming $d = 30$ m, $\frac{P}{N_o} = 25$ dB, $\gamma_{th} = 5$, $\alpha = 2$ and $\mu = 4$. As a benchmark, the corresponding outage probability in the case in which there is no misalignment fading is also plotted. From this figure, we observe that for a given κ_{tr}, as σ_s increases, i.e., as the impact of misalignment becomes
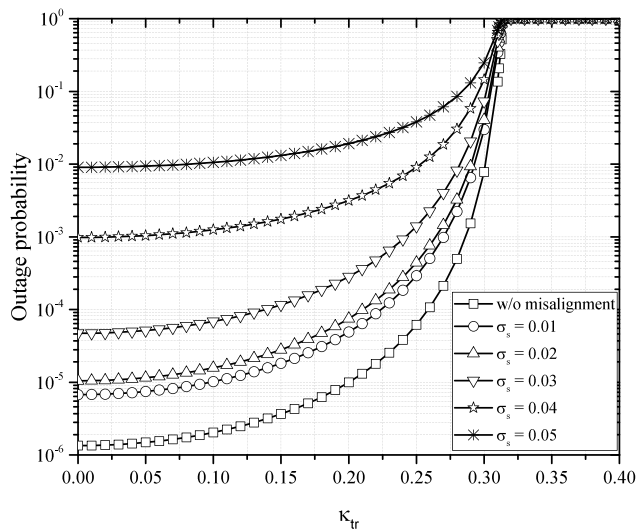
more severe, the outage probability also increases. For example, for $\kappa_{tr} = 0.10$, the outage probability increases from 10^{-5} to 1.25×10^{-3}, as σ_s shifts from 0.01 to 0.04 m. Moreover, in the low σ_s regime, it is shown that the outage performance degradation created by the RF imperfections is somewhat more severe compared with the detrimental effects of misalignment fading. For instance, for the case of $\kappa_{tr} = 0.10$, the doubling of the level of misalignment from 0.01 to 0.02 m causes a 54.58% outage probability degradation, whereas, for $\sigma_s = 0.01$ m, the doubling of the level of hardware imperfections from $\kappa_{tr} = 0.10$ to 0.20 results to a 381.01% outage probability degradation. On the other hand, in the relatively high σ_s regime, the outage performance degradation created by the RF imperfections is somewhat less severe compared with the detrimental effects of misalignment fading. Finally, in the case of ideal RF front-end, i.e., $\kappa_{tr} = 0$, the assumption of perfect transceivers alignment results to around 402.19% error in the corresponding outage probability for $\sigma_s = 0.01$ m. These results highlight the importance of both accurate misalignment characterization and accounting for RF impairments in the realistic performance analysis and design of THz wireless fiber extender systems.

In Fig. 13, the ergodic capacity is plotted as a function $\frac{P}{N_o}$, for different values of κ_{tr}, assuming $d = 30$ m, $\sigma_s = 0.01$ m, $\alpha = 2$ and $\mu = 4$. In this figure, the continuous lines represent Monte Carlo simulation results, while the dashed lines stand for the capacity upper bound, which is derived by (54) and (55). Additionally, the dashed-dotted lines denote the capacity ceiling, given by (59). Note that, as a benchmark, the capacity versus $\frac{P}{N_o}$ for the ideal RF chains case is also plotted. As expected, as $\frac{P}{N_o}$ increases, the ergodic capacity also increases. However, in the case of non-ideal RF chains, the ergodic capacity saturates as it approaches the capacity ceiling, as proven from Lemma 3. As a result, since the

FIGURE 12. Outage probability vs κ_{tr}, for different values of σ_s, assuming $d = 30$ m, $\frac{P}{N_o} = 25$ dB, $\gamma_{th} = 5$, $\alpha = 2$ and $\mu = 4$.
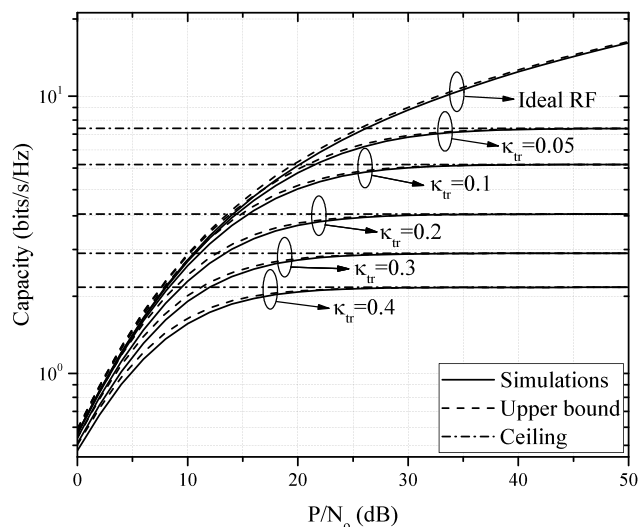

FIGURE 13. Capacity vs $\frac{P}{N_o}$, for different values of κ_{tr}, assuming $d = 30$ m, $\sigma_s = 0.01$ m, $\alpha = 2$ and $\mu = 4$.

capacity ceiling is determined by the level of imperfections, it increases as κ_{tr} decreases. Moreover, we observe that the hardware imperfections have a small effect on the ergodic capacity at the low $\frac{P}{N_o}$ regime, whereas, at the high $\frac{P}{N_o}$ regime their impact is detrimental. Finally, from this figure, it is evident that the upper bounds derived by Theorems 4 and 5 are relatively tight; especially, in the high $\frac{P}{N_o}$ regime.

VI. CONCLUSIONS

We studied the performance of wireless THz fiber extenders, when the RF front-end is impaired by hardware imperfections and the transceivers antennas are not fully-aligned. In particular, by assuming $\alpha - \mu$ fading and Gaussian distributions for the elevation and horizontal displacement, we provided a general analytical framework for evaluating the outage probability for both cases of ideal and non-ideal RF front-end. Next, we presented novel closed-form expressions for the ergodic capacity in the case of ideal RF front-end as well as upper bounds for both cases of ideal and non-ideal RF front-end. Likewise, a simple capacity ceiling for the non-ideal RF front-end case was extracted. Our results illustrated the degradation due to the joint effect of misalignment fading and RF imperfections on the outage and capacity performance of the THz wireless extender. Among other, it was revealed that the impact of misalignment fading is somewhat more detrimental compared to the one of the multipath fading, whereas the performance degradation created by the RF imperfections is more severe compared with the detrimental effect of misalignment fading. Finally, the importance of both accurate misalignment characterization and accounting for RF impairments in the realistic performance analysis and design of THz wireless fiber extenders was highlighted.

APPENDIX A
PROOF OF THEOREM 1

According to [91], the PDF of $|h_{fp}|$ can be obtained as

$$f_{|h_{fp}|}(x) = \int_0^{A_o} \frac{1}{y} f_{|h_f|}\left(\frac{x}{y}\right) f_{|h_m|}(y) \mathrm{d}y. \tag{62}$$

By substituting (22) and (24) into (62) and after some algebraic manipulations, the PDF of $|h_{fp}|$ can be equivalently expressed as

$$f_{|h_{fp}|}(x) = \frac{\alpha \mu^\mu x^{\alpha\mu-1}}{\left(\hat{h}_f\right)^{\alpha\mu} \Gamma(\mu)} \frac{\gamma^2}{A_o^{\gamma^2}} \mathcal{I}(x), \tag{63}$$

where

$$\mathcal{I}(x) = \int_0^{A_o} y^{\gamma^2-\alpha\mu-1} \exp\left(-\mu \frac{x^\alpha y^{-\alpha}}{\hat{h}^\alpha}\right) \mathrm{d}y, \tag{64}$$

which, by employing [64, eq. (8/350/1)], can be rewritten as in (26). This concludes the proof.

APPENDIX B
PROOF OF THEOREM 2

Since $|h_f|$ and $|h_p|$ are independent random variables, the CDF of $|h_{fp}|$ can be derived as

$$F_{|h_{fp}|}(x) = \int_0^{A_o} F_{|h_f|}\left(\frac{x}{y}\right) f_{|h_p|}(y) \mathrm{d}y, \tag{65}$$

where $f_{|h_p|}(x)$ is the PDF of $|h_p|$, while $F_{|h_f|}(x)$ stand for the CDF of $|h_f|$. Since $|h_f|$ follows α-μ distribution, its CDF can be expressed as [83, eq. (8)]

$$F_{|h_f|}(x) = 1 - \frac{\Gamma\left(\mu, \mu \frac{x^\alpha}{\hat{h}_f^\alpha}\right)}{\Gamma(\mu)}, \tag{66}$$

which, by assuming that μ is an integer and employing [64, eq. (8.352/2)], (66) can be rewritten as

$$F_{|h_f|}(x) = 1 - \sum_{k=0}^{\mu-1} \frac{1}{k!}\left(\mu \frac{x^\alpha}{\hat{h}_f^\alpha}\right)^k \exp\left(-\mu \frac{x^\alpha}{\hat{h}_f^\alpha}\right). \tag{67}$$

Moreover, by substituting (22) and (67) into (65), the CDF of $|h_{fp}|$ can be equivalently expressed as

$$F_{|h_{fp}|}(x) = \mathcal{K} - \sum_{k=0}^{\mu-1} \mathcal{J}_k(x), \tag{68}$$

where

$$\mathcal{K} = \int_0^{A_o} f_{|h_p|}(y) \mathrm{d}y \tag{69}$$

and

$$\mathcal{J}_k(x) = \frac{\mu^k}{k!} \frac{x^{\alpha k}}{\left(\hat{h}_f\right)^{\alpha k}} \frac{\gamma^2}{A_o^{\gamma^2}}$$
$$\times \int_0^{A_o} y^{\gamma^2-\alpha k-1} \exp\left(-\mu \frac{x^\alpha}{\hat{h}_f^\alpha} y^{-\alpha}\right) \mathrm{d}y. \tag{70}$$

Next, we evaluate each term that composes (68). Since $f_{|h_p|}(y)$ represents the PDF of $|h_p|$,

$$\mathcal{K} = 1. \tag{71}$$

Moreover, by setting

$$z = \mathcal{A}(x) y^{-\alpha}, \tag{72}$$

with

$$\mathcal{A}(x) = \mu \frac{x^\alpha}{\hat{h}_f^\alpha}, \tag{73}$$

(70) can be rewritten as

$$\mathcal{J}_k(x) = \frac{\mu^k}{k!} \frac{x^{\alpha k}}{\left(\hat{h}_f\right)^{\alpha k}} \frac{\gamma^2}{A_o^{\gamma^2}} \frac{\left(\mathcal{A}(x)\right)^{\frac{\gamma^2-\alpha k}{\kappa}}}{\alpha}$$
$$\times \int_{\frac{\mathcal{A}(x)}{A_o^\alpha}}^\infty z^{-\frac{\gamma^2-\alpha k}{\alpha}-1} \exp\left(-z\right) \mathrm{d}z, \tag{74}$$

which, according to [64, eq. (8.350/2)], can be evaluated as

$$\mathcal{J}_k(x) = \frac{\mu^k}{k!} \frac{x^{\alpha k}}{\left(\hat{h}_f\right)^{\alpha k}} \frac{\gamma^2}{A_o^{\gamma^2}} \frac{(\mathcal{A}(x))^{\frac{\gamma^2 - \alpha k}{\alpha}}}{\alpha}$$
$$\times \Gamma\left(\frac{\alpha k - \gamma^2}{\alpha}, \frac{\mathcal{A}(x)}{A_o^\alpha}\right). \quad (75)$$

Additionally, by employing (73), (75) can be expressed as

$$\mathcal{J}_k(x) = \frac{1}{\alpha} \frac{\mu^{k + \frac{\gamma^2 - \alpha k}{\alpha}}}{k!} \frac{x^{\gamma^2}}{\hat{h}_f^{\gamma^2}} \frac{\gamma^2}{A_o^{\gamma^2}} \Gamma\left(\frac{\alpha k - \gamma^2}{\alpha}, \frac{\mu \frac{x^\alpha}{\hat{h}_f^\alpha}}{A_o^\alpha}\right). \quad (76)$$

Finally, by substituting (71) and (76) into (68), and after some algebraic manipulations, we get (27). This concludes the proof.

APPENDIX C
PROOF OF PROPOSITION 2
In the case of non-ideal RF front-end, the outage probability can be defined as

$$P_o(\gamma_{th}) = P_r(\rho \leq \gamma_{th}), \quad (77)$$

which, based on (38), can be rewritten as

$$P_o(\gamma_{th}) = P_r\left(\frac{|h|^2 P}{\kappa^2 |h|^2 P + N_o} \leq \gamma_{th}\right), \quad (78)$$

or equivalently

$$P_o(\gamma_{th}) = P_r\left(|h|^2 P\left(1 - \kappa^2 \gamma_{th}\right) \leq N_o\right). \quad (79)$$

By employing (4), (79) can be expressed as

$$P_o(\gamma_{th}) = P_r\left(|h_{fp}|^2\left(1 - \kappa^2 \gamma_{th}\right) \leq \frac{N_o}{P|h_l|^2}\right). \quad (80)$$

Moreover, by assuming that $1 - \kappa^2 \gamma_{th} \geq 0$, i.e., $\gamma_{th} \leq \frac{1}{\kappa^2}$, the outage probability can be derived as

$$P_o(\gamma_{th}) = P_r\left(|h_{fp}|^2 \leq \frac{N_o}{P|h_l|^2\left(1 - \kappa^2 \gamma_{th}\right)}\right), \quad (81)$$

or

$$P_o(\gamma_{th}) = F_{|h_{fp}|}\left(\sqrt{\frac{N_o}{P|h_l|^2\left(1 - \kappa^2 \gamma_{th}\right)}}\right). \quad (82)$$

Finally, if $1 - \kappa^2 \gamma_{th} < 0$, then the condition

$$|h_{fp}|^2\left(1 - \kappa^2 \gamma_{th}\right) \leq 0 \leq \frac{N_o}{P|h_l|^2} \quad (83)$$

is always valid and the outage probability equals 1. This concludes the proof.

APPENDIX D
PROOF OF LEMMA 2
Similar to (82), in the absence of misalignment fading, if $1 - \kappa^2 \gamma_{th} \geq 0$ the outage probability can be expressed as

$$P_o^{wm}(\gamma_{th}) = P_r\left(|h_f| \leq \sqrt{\frac{N_o}{P|h_l|^2\left(1 - \kappa^2 \gamma_{th}\right)}}\right), \quad (84)$$

or equivalently

$$P_o^{wm}(\gamma_{th}) = F_{|h_f|}\left(\sqrt{\frac{N_o}{P|h_l|^2\left(1 - \kappa^2 \gamma_{th}\right)}}\right), \quad (85)$$

which, by using (66), can be rewritten as (47). Moreover, if $1 - \kappa^2 \gamma_{th} < 0$, then, similarly to (83), it can be proven that the outage probability equals 1. This concludes the proof.

APPENDIX E
PROOF OF THEOREM 3
In the case of ideal RF front-end, the ergodic capacity can be defined as

$$C_{id} = \mathbb{E}\left[\log_2(1 + \rho)\right], \quad (86)$$

or

$$C_{id} = \mathbb{E}\left[\log_2\left(1 + \mathcal{P}|h_{fp}|^2\right)\right], \quad (87)$$

which can be evaluated as

$$C_{id} = \int_0^\infty \log_2\left(1 + \mathcal{P}x^2\right) f_{|h_{fp}|}(x)\mathrm{d}x. \quad (88)$$

By substituting (26) into (88), and after some algebraic manipulations, the ergodic capacity can be expressed as

$$C_{id} = \frac{\Xi}{\ln(2)} \int_0^\infty x^{\mathcal{B}} \ln\left(1 + \mathcal{P}x^2\right) \Gamma\left(K, Lx^\alpha\right) \mathrm{d}x, \quad (89)$$

or, by using [65, eq. (15.1.1)], as

$$C_{id} = \frac{\Xi}{\ln(2)} \int_0^\infty x^{\mathcal{B}+1} {}_2F_1[1, 1; 2; -x] \Gamma\left(K, Lx^\alpha\right) \mathrm{d}x. \quad (90)$$

Moreover, by employing [64, eq. (9.34/7)] and [92, eq. (11)], (90) can be written as

$$C_{id} = \frac{\Xi}{\ln(2)} \int_0^\infty x^{\mathcal{B}} G_{2,2}^{1,2}\left[\mathcal{P}x^2 \,\middle|\, \begin{matrix} 1, 1 \\ 1, 0 \end{matrix}\right] \times G_{1,2}^{2,0}\left[Lx^\alpha \,\middle|\, \begin{matrix} 1 \\ 0, K \end{matrix}\right] \mathrm{d}x, \quad (91)$$

which, by setting $z = x^2$, can be expressed as

$$C_{id} = \frac{\Xi}{2\ln(2)} \int_0^\infty z^{\frac{\mathcal{B}+1}{2} - 1} G_{2,2}^{1,2}\left[\mathcal{P}z \,\middle|\, \begin{matrix} 1, 1 \\ 1, 0 \end{matrix}\right] \times G_{1,2}^{2,0}\left[Lz^{\frac{\alpha}{2}} \,\middle|\, \begin{matrix} 1 \\ 0, K \end{matrix}\right] \mathrm{d}z. \quad (92)$$

Finally, by using [93] into (92), the ergodic capacity can be rewritten as (48). This concludes the proof.

APPENDIX F
PROOF OF THEOREM 4

Based on (86), the ergodic capacity can be rewritten as

$$C_{id} = \mathbb{E}\left[\log_2\left(1 + \frac{p}{N_o}\right)\right], \tag{93}$$

where

$$p = |h|^2 P. \tag{94}$$

By applying Jensen's inequality [86] into (93), we can upper-bound the ergodic capacity as

$$C \leq \log_2\left(1 + \frac{\mathbb{E}[p]}{N_o}\right). \tag{95}$$

Next, we analytically evaluate $\mathbb{E}[p]$. Since $|h_p|$ and $|h_f|$ are independent random variables, $|h_p|^2$ and $|h_f|^2$ are also independent random variables; hence,

$$\mathbb{E}[p] = P\mathbb{E}\left[|h_l|^2|h_f|^2|h_p|^2\right], \tag{96}$$

can be rewritten as

$$\mathbb{E}[p] = P|h_l|^2\mathbb{E}\left[|h_f|^2\right]\mathbb{E}\left[|h_p|^2\right]. \tag{97}$$

The expected value of $|h_f|^2$ can be evaluated as

$$\mathbb{E}\left[|h_f|^2\right] = \int_0^\infty x^2 f_{|h_f|}(x)\mathrm{d}x, \tag{98}$$

which, by employing (24), can be equivalently written as

$$\mathbb{E}\left[|h_f|^2\right] = \frac{\alpha\mu^\mu}{\hat{h}_f^{\alpha\mu}\Gamma(\mu)}\mathcal{L}, \tag{99}$$

where

$$\mathcal{L} = \int_0^\infty x^{\alpha\mu+1}\exp\left(-\mu\frac{x^\alpha}{\hat{h}_f^\alpha}\right)\mathrm{d}x. \tag{100}$$

By setting $u = \mu\frac{x^\alpha}{\hat{h}_f^\alpha}$ and employing [64, eq. (8.350/2)], (100) can be analytically evaluated as

$$\mathcal{L} = \frac{1}{\alpha}\left(\frac{\mu}{\hat{h}_f^\alpha}\right)^{-\frac{\alpha\mu+2}{\alpha}}\Gamma\left(\frac{2}{\alpha} + \mu\right). \tag{101}$$

By substituting (101) into (99), we can express the expected value of $|h_f|^2$ as

$$\mathbb{E}\left[|h_f|^2\right] = \frac{\hat{h}_f^2}{\mu^{\frac{2}{\alpha}}}\frac{\Gamma\left(\frac{2}{\alpha} + \mu\right)}{\Gamma(\mu)}. \tag{102}$$

Similarly, the expected value of $|h_p|^2$ can be evaluated as

$$\mathbb{E}\left[|h_p|^2\right] = \int_0^{A_o} x^2 f_{|h_p|}(x)\mathrm{d}x, \tag{103}$$

which, by employing (22), can be rewritten as

$$\mathbb{E}\left[|h_p|^2\right] = \frac{\gamma^2}{A_o^{\gamma^2}}\int_0^{A_o} x^{\gamma^2+1}\mathrm{d}x, \tag{104}$$

or

$$\mathbb{E}\left[|h_p|^2\right] = \frac{\gamma^2}{2 + \gamma^2}A_o^2. \tag{105}$$

Moreover, by using (105) and (102), (97) can be written as

$$\mathbb{E}[p] = P|h_l|^2\frac{\gamma^2 A_o^2}{2 + \gamma^2}\frac{\hat{h}_f^2}{\mu^{\frac{2}{\alpha}}}\frac{\Gamma\left(\frac{2}{\alpha} + \mu\right)}{\Gamma(\mu)}. \tag{106}$$

Finally, by substituting (106) into (95), we get (54). This concludes the proof.

REFERENCES

[1] M. Agiwal, A. Roy, and N. Saxena, "Next generation 5G wireless networks: A comprehensive survey," *IEEE Commun. Surveys Tuts.*, vol. 18, no. 3, pp. 1617–1655, 3rd Quart., 2016.

[2] A.-A. A. Boulogeorgos and G. K. Karagiannidis, "Low-cost cognitive radios against spectrum scarcity," *IEEE Tech. Committee Cogn. Netw. Newslett.*, vol. 3, no. 2, pp. 30–34, Nov. 2017.

[3] A.-A. A. Boulogeorgos, "Interference mitigation techniques in modern wireless communication systems," Ph.D. dissertation, Dept. Elect. Comput. Eng., Aristotle Univ. Thessaloniki, Thessaloniki, Greece, Sep. 2016.

[4] A.-A. A. Boulogeorgos *et al.*, "Terahertz technologies to deliver optical network quality of experience in wireless systems beyond 5G," *IEEE Commun. Mag.*, vol. 56, no. 6, pp. 144–151, Jun. 2018.

[5] H. Shokri-Ghadikolaei *et al.*, "Millimeter wave cellular networks: A MAC layer perspective," *IEEE Trans. Commun.*, vol. 63, no. 10, pp. 3437–3458, Oct. 2015.

[6] I. F. Akyildiz, J. M. Jornet, and C. Han, "Terahertz band: Next frontier for wireless communications," *Phys. Commun.*, vol. 12, pp. 16–32, Sep. 2014.

[7] C. Zhang, K. Ota, J. Jia, and M. Dong, "Breaking the blockage for big data transmission: Gigabit road communication in autonomous vehicles," *IEEE Commun. Mag.*, vol. 56, no. 6, pp. 152–157, Jun. 2018.

[8] A.-A. A. Boulogeorgos *et al.*, "Wireless terahertz system architectures for networks beyond 5G," Terranova Consortium, White Paper 1.0, Jul. 2018.

[9] C. Han and Y. Chen, "Propagation modeling for wireless communications in the terahertz band," *IEEE Commun. Mag.*, vol. 56, no. 6, pp. 96–101, Jun. 2018.

[10] G. A. Siles, J. M. Riera, and P. García-del-Pino, "Atmospheric attenuation in wireless communication systems at millimeter and THz frequencies," *IEEE Antennas Propag. Mag.*, vol. 57, no. 1, pp. 48–61, Feb. 2015.

[11] P. Boronin, V. Petrov, D. Moltchanov, Y. Koucheryavy, and J. M. Jornet, "Capacity and throughput analysis of nanoscale machine communication through transparency windows in the terahertz band," *Nano Commun. Netw.*, vol. 5, no. 3, pp. 72–82, Sep. 2014.

[12] J. M. Jornet and I. F. Akyildiz, "Channel capacity of electromagnetic nanonetworks in the terahertz band," in *Proc. IEEE Int. Conf. Commun. (ICC)*, Cape Town, South Africa, May 2010, pp. 1–6.

[13] C. Lin and G. Y. Li, "Terahertz communications: An array-of-subarrays solution," *IEEE Commun. Mag.*, vol. 54, no. 12, pp. 124–131, Dec. 2016.

[14] K. Guan *et al.*, "On millimeter wave and THz mobile radio channel for smart rail mobility," *IEEE Trans. Veh. Technol.*, vol. 66, no. 7, pp. 5658–5674, Jul. 2017.

[15] A.-A. A. Boulogeorgos, E. Papasotiriou, and A. Alexiou, "A distance and bandwidth dependent adaptive modulation scheme for THz communications," in *Proc. 19th IEEE Int. Workshop Signal Process. Adv. Wireless Commun. (SPAWC)*, Kalamata, Greece, Jul. 2018, pp. 1–5.

[16] A.-A. A. Boulogeorgos, S. Goudos, and A. Alexiou, "Users association in ultra dense THz networks," in *Proc. IEEE Int. Workshop Signal Process. Adv. Wireless Commun. (SPAWC)*, Kalamata, Greece, Jun. 2018, pp. 1–5.

[17] N. Akkari *et al.*, "Joint physical and link layer error control analysis for nanonetworks in the terahertz band," *Wireless Netw.*, vol. 22, no. 4, pp. 1221–1233, May 2016.

[18] S. Han, C.-L. I, Z. Xu, and C. Rowell, "Large-scale antenna systems with hybrid analog and digital beamforming for millimeter wave 5G," *IEEE Commun. Mag.*, vol. 53, no. 1, pp. 186–194, Jan. 2015.

[19] A. S. Cacciapuoti, K. Sankhe, M. Caleffi, and K. R. Chowdhury, "Beyond 5G: THz-based medium access protocol for mobile heterogeneous networks," *IEEE Commun. Mag.*, vol. 56, no. 6, pp. 110–115, Jun. 2018.

[20] P. Rykaczewski, M. Valkama, and M. Renfors, "On the connection of I/Q imbalance and channel equalization in direct-conversion transceivers," *IEEE Trans. Veh. Technol.*, vol. 57, no. 3, pp. 1630–1636, May 2008.

[21] J. M. Jornet and I. F. Akyildiz, "Channel modeling and capacity analysis for electromagnetic wireless nanonetworks in the terahertz band," *IEEE Trans. Wireless Commun.*, vol. 10, no. 10, pp. 3211–3221, Oct. 2011.

[22] K. Yang, A. Pellegrini, M. Munoz, A. Brizzi, A. Alomainy, and Y. Hao, "Numerical analysis and characterization of THz propagation channel for body-centric nano-communications," *IEEE Trans. THz Sci. Technol.*, vol. 5, no. 3, pp. 419–426, May 2015.

[23] J. Kokkoniemi, J. Lehtomäki, and M. Juntti, "Simplified molecular absorption loss model for 275–400 gigahertz frequency band," in *Proc. 12th Eur. Conf. Antennas Propag. (EuCAP)*, London, U.K., Apr. 2018, pp. 1–5.

[24] A.-A. A. Boulogeorgos, E. N. Papasotiriou, J. Kokkoniemi, J. Lehtomäki, A. Alexiou, and M. Juntti, "Performance evaluation of THz wireless systems operating in 275-400 GHz band," in *Proc. IEEE Veh. Technol. Conf. (VTC)*, Jun. 2018, pp. 1–5.

[25] E. N. Papasotiriou, J. Kokkoniemi, A.-A. A. Boulogeorgos, J. Lehtomäki, A. Alexiou, and M. Juntti, "A new look to 275 to 400 GHz band: Channel model and performance evaluation," in *Proc. IEEE Int. Symp. Pers., Indoor Mobile Radio Commun. (PIMRC)*, Bolonia, Italy, Sep. 2018, pp. 1–5.

[26] A. Afsharinejad, A. Davy, B. Jennings, and C. Brennan, "An initial path-loss model within vegetation in the THz band," in *Proc. 9th Eur. Conf. Antennas Propag. (EuCAP)*, Lisbon, Portugal, May 2015, pp. 1–5.

[27] H. Elayan, R. M. Shubair, J. M. Jornet, and P. Johari, "Terahertz channel model and link budget analysis for intrabody nanoscale communication," *IEEE Trans. Nanobiosci.*, vol. 16, no. 6, pp. 491–503, Sep. 2017.

[28] M. A. Akka , "Terahertz channel modelling of wireless ultra-compact sensor networks using electromagnetic waves," *IET Commun.*, vol. 10, no. 13, pp. 1665–1672, 2016.

[29] C. Han, A. O. Bicen, and I. F. Akyildiz, "Multi-ray channel modeling and wideband characterization for wireless communications in the terahertz band," *IEEE Trans. Wireless Commun.*, vol. 14, no. 5, pp. 2402–2412, May 2015.

[30] J. Kokkoniemi, J. Lehtomäki, and M. Juntti, "Frequency domain scattering loss in THz band," in *Proc. Global Symp. Millim.-Waves (GSMM)*, Montreal, QC, Canada, May 2015, pp. 1–3.

[31] A. R. Ekti *et al.*, "Statistical modeling of propagation channels for terahertz band," in *Proc. IEEE Conf. Standards Commun. Netw. (CSCN)*, Helsinki, Finland, Sep. 2017, pp. 275–280.

[32] S. Priebe, C. Jastrow, M. Jacob, T. Kleine-Ostmann, T. Schrader, and T. Kurner, "Channel and propagation measurements at 300 GHz," *IEEE Trans. Antennas Propag.*, vol. 59, no. 5, pp. 1688–1698, May 2011.

[33] S. Kim and A. Zajić, "Statistical modeling of THz scatter channels," in *Proc. 9th Eur. Conf. Antennas Propag. (EuCAP)*, Lisbon, Portugal, May 2015, pp. 1–5.

[34] S. Kim and A. Zajić, "Statistical modeling and simulation of short-range device-to-device communication channels at sub-THz frequencies," *IEEE Trans. Wireless Commun.*, vol. 15, no. 9, pp. 6423–6433, Sep. 2016.

[35] S. Priebe, M. Jacob, and T. Kürner, "The impact of antenna directivities on THz indoor channel characteristics," in *Proc. 6th Eur. Conf. Antennas Propag. (EUCAP)*, Prague, Czech Republic, Mar. 2012, pp. 478–482.

[36] A. Afsharinejad, A. Davy, B. Jennings, S. Rasmann, and C. Brennan, "A path-loss model incorporating shadowing for THz band propagation in vegetation," in *Proc. Global Commun. Conf. (GLOBECOM)*, San Diego, CA, USA, Dec. 2015, pp. 1–6.

[37] C. Han and I. F. Akyildiz, "Three-dimensional end-to-end modeling and analysis for graphene-enabled terahertz band communications," *IEEE Trans. Veh. Technol.*, vol. 66, no. 7, pp. 5626–5634, Jul. 2017.

[38] V. Petrov, A. Pyattaev, D. Moltchanov, and Y. Koucheryavy, "Terahertz band communications: Applications, research challenges, and standardization activities," in *Proc. 8th Int. Congr. Ultra Mod. Telecommun. Control Syst. Workshops (ICUMT)*, Lisbon, Portugal, pp. 183–190, Oct. 2016.

[39] C. Liu, Y. Yao, Y. Sun, and X. Zhao, "Average capacity for heterodyne FSO communication systems over gamma-gamma turbulence channels with pointing errors," *Electron. Lett.*, vol. 46, no. 12, pp. 851–853, Jun. 2010.

[40] A. J. Seeds, H. Shams, M. J. Fice, and C. C. Renaud, "Terahertz photonics for wireless communications," *J. Lightw. Technol.*, vol. 33, no. 3, pp. 579–587, Feb. 1, 2015.

[41] S. Koenig *et al.*, "Wireless sub-THz communication system with high data rate," *Nature Photon.*, vol. 7, p. 977, Oct. 2013.

[42] T. Nagatsuma, G. Ducournau, and C. C. Renaud, "Advances in terahertz communications accelerated by photonics," *Nature Photon.*, vol. 10, p. 371, May 2016.

[43] M. Elkhouly, Y. Mao, S. Glisic, C. Meliani, F. Ellinger, and J. C. Scheytt, "A 240 GHz direct conversion IQ receiver in 0.13 μm SiGe BiCMOS technology," in *Proc. IEEE Radio Freq. Integr. Circuits Symp. (RFIC)*, Seattle, WA, USA, Jun. 2013, pp. 305–308.

[44] I. Kallfass *et al.*, "Towards MMIC-based 300 GHz indoor wireless communication systems," *IEICE Trans. Electron.*, vol. 98, no. 12, pp. 1081–1090, Dec. 2015.

[45] T. Schenk, *RF Imperfections in High-rate Wireless Systems: Impact and Digital Compensation*. Dordrecht, The Netherlands: Springer, 2008.

[46] A. A. Abidi, "Direct-conversion radio transceivers for digital communications," *IEEE J. Solid-State Circuits*, vol. 30, no. 12, pp. 1399–1410, Dec. 1995.

[47] A.-A. A. Boulogeorgos, V. M. Kapinas, R. Schober, and G. K. Karagiannidis, "I/Q-imbalance self-interference coordination," *IEEE Trans. Wireless Commun.*, vol. 15, no. 6, pp. 4157–4170, Jun. 2016.

[48] A.-A. A. Boulogeorgos, P. C. Sofotasios, S. Muhaidat, M. Valkama, and G. K. Karagiannidis, "The effects of RF impairments in vehicle-to-vehicle communications," in *Proc. IEEE 25th Int. Symp. Pers., Indoor Mobile Radio Commun. (PIMRC)*, Hong Kong, Aug. 2015, pp. 840–845.

[49] A.-A. A. Boulogeorgos, P. C. Sofotasios, B. Selim, S. Muhaidat, G. K. Karagiannidis, and M. Valkama, "Effects of RF impairments in communications over cascaded fading channels," *IEEE Trans. Veh. Technol.*, vol. 65, no. 11, pp. 8878–8894, Nov. 2016.

[50] A.-A. A. Boulogeorgos, H. A. B. Salameh, and G. K. Karagiannidis, "On the effects of I/Q imbalance on sensing performance in Full-Duplex cognitive radios," in *Proc. IEEE Wireless Commun. Netw. Conf. (WCNC) Int. Workshop Smart Spectr. (IWSS) (WCNC-IWSS)*, Doha, Qatar, Apr. 2016, pp. 361–366.

[51] M. Mokhtar, A.-A. A. Boulogeorgos, G. K. Karagiannidis, and N. Al-Dhahir, "OFDM opportunistic relaying under joint transmit/receive I/Q imbalance," *IEEE Trans. Commun*, vol. 62, no. 5, pp. 1458–1468, Jul. 2014.

[52] E. Björnson, M. Matthaiou, and M. Debbah, "Massive MIMO systems with hardware-constrained base stations," in *Proc. IEEE Int. Conf. Acoust., Speech Signal Process. (ICASSP)*, Florence, Italy, May 2014, pp. 3142–3146.

[53] A. Gokceoglu, Y. Zou, M. Valkama, and P. C. Sofotasios, "Multi-channel energy detection under phase noise: Analysis and mitigation," *Mobile Netw. Appl.*, vol. 19, no. 4, pp. 473–486, May 2014.

[54] A. Gokceoglu, S. Dikmese, M. Valkama, and M. Renfors, "Energy detection under IQ imbalance with single- and multi-channel direct-conversion receiver: Analysis and mitigation," *IEEE J. Sel. Areas Commun.*, vol. 32, no. 3, pp. 411–424, Mar. 2014.

[55] A.-A. A. Boulogeorgos, N. Chatzidiamantis, G. K. Karagiannidis, and L. Georgiadis, "Energy detection under RF impairments for cognitive radio," in *Proc. IEEE Int. Conf. Commun.-Workshop Cooperat. Cogn. Netw. (ICC-CoCoNet)*, London, U.K., Jun. 2015, pp. 955–960.

[56] L. Anttila, M. Valkama, and M. Renfors, "Frequency-selective I/Q mismatch calibration of wideband direct-conversion transmitters," *IEEE Trans. Circuits Syst. II, Exp. Briefs*, vol. 55, no. 4, pp. 359–363, Apr. 2008.

[57] L. Anttila, M. Valkama, and M. Renfors, "Circularity-based I/Q imbalance compensation in Wideband direct-conversion receivers," *IEEE Trans. Veh. Tech.*, vol. 57, no. 4, pp. 2099–2113, Jul. 2008.

[58] E. Björnson, P. Zetterberg, and M. Bengtsson, "Optimal coordinated beamforming in the multicell downlink with transceiver impairments," in *Proc. IEEE Global Commun. Conf.*, Anaheim, CA, USA, Dec. 2012, pp. 4775–4780.

[59] T. T. Duy, T. Q. Duong, D. B. da Costa, V. N. Q. Bao, and M. Elkashlan, "Proactive relay selection with joint impact of hardware impairment and co-channel interference," *IEEE Trans. Commun.*, vol. 63, no. 5, pp. 1594–1606, May 2015.

[60] A. Gokceoglu, Y. Zou, M. Valkama, P. C. Sofotasios, P. Mathecken, and D. Cabric, "Mutual information analysis of OFDM radio link under phase noise, IQ imbalance and frequency-selective fading channel," *IEEE Trans. Wireless Commun.*, vol. 12, no. 6, pp. 3048–3059, Jun. 2013.

[61] E. Björnson, A. Papadogiannis, M. Matthaiou, and M. Debbah, "On the impact of transceiver impairments on AF relaying," in *Proc. IEEE Int. Conf. Acoust., Speech Signal Process. (ICASSP)*, Vancouver, BC, Canada, May 2013, pp. 4948–4952.

[62] V. A. Aalo, T. Piboongungon, and C. D. Iskander, "Bit-error rate of binary digital modulation schemes in generalized gamma fading channels," *IEEE Commun. Lett.*, vol. 9, no. 2, pp. 139–141, Feb. 2005.

[63] E. J. Leonardo, M. D. Yacoub, and R. A. A. de Souza, "Ratio of products of α-μ variates," *IEEE Commun. Lett.*, vol. 20, no. 5, pp. 1022–1025, May 2016.

[64] I. S. Gradshteĭyn and I. M. Ryzhik, *Table of Integrals, Series, and Products*, 6th ed. New York, NY, USA: Academic, 2000.

[65] M. Abramowitz and I. A. Stegun, Eds., *Handbook of Mathematical Functions: With Formulas, Graphs, and Mathematical Tables*, 9th ed. New York, NY, USA: Dover, 1972.

[66] A. P. Prudnikov, Y. A. Brychkov, and O. I. Marichev, *Integral Series: More Special Functions*, vol. 3. Boca Raton, FL, USA: CRC Press, 1990.

[67] E. Björnson, M. Matthaiou, and M. Debbah, "A new look at dual-hop relaying: Performance limits with hardware impairments," *IEEE Trans. Commun.*, vol. 61, no. 11, pp. 4512–4525, Nov. 2013.

[68] C. Studer, M. Wenk, and A. Burg, "MIMO transmission with residual transmit-RF impairments," in *Proc. Int. ITG Workshop Smart Antennas (WSA)*, Feb. 2010, pp. 189–196.

[69] M. Wenk, *MIMO-OFDM Testbed: Challenges, Implementations, and Measurement Results* (Series in Microelectronics). Zürich, Switzerland: ETH Zürich, 2010.

[70] D. Dardari, V. Tralli, and A. Vaccari, "A theoretical characterization of nonlinear distortion effects in OFDM systems," *IEEE Trans. Commun.*, vol. 48, no. 10, pp. 1755–1764, Oct. 2000.

[71] B. E. Priyanto, T. B. Sorensen, O. K. Jensen, T. Larsen, T. Kolding, and P. Mogensen, "Assessing and modeling the effect of RF impairments on UTRA LTE uplink performance," in *Proc. IEEE 66th Veh. Technol. Conf.*, Baltimore, MD, USA, Sep. 2007, pp. 1213–1217.

[72] A.-A. A. Boulogeorgos, N. D. Chatzidiamantis, and G. K. Karagiannidis, "Energy detection spectrum sensing under RF imperfections," *IEEE Trans. Commun.*, vol. 64, no. 7, pp. 2754–2766, Jul. 2016.

[73] T. L. Jensen and T. Larsen, "Robust computation of error vector magnitude for wireless standards," *IEEE Trans. Commun.*, vol. 61, no. 2, pp. 648–657, Feb. 2013.

[74] *8 Hints for Making and Interpreting EVM Measurements*, Agilent Technol., Santa Clara, CA, USA, 2005.

[75] C. A. Balanis, *Modern Antenna Handbook*. New York, NY, USA: Wiley, 2008.

[76] R. M. Goody and Y. L. Yung, *Atmospheric Radiation: Theoretical Basis*. London, U.K.: Oxford Univ. Press, 1995.

[77] E. A. L. S. Rothman, "The HITRAN 2008 molecular spectroscopic database," *J. Quant. Spectrosc. Radiat. Transf.*, vol. 110, nos. 9–10, pp. 533–572, Jun. 2009.

[78] O. A. Alduchov and R. E. Eskridge, "Improved magnus form approximation of saturation vapor pressure," *J. Appl. Meteorol.*, vol. 35, no. 4, pp. 601–609, 1996.

[79] A. A. Farid and S. Hranilovic, "Outage capacity optimization for free-space optical links with pointing errors," *J. Lightw. Technol.*, vol. 25, no. 7, pp. 1702–1710, Jul. 2007.

[80] S. Arnon, "Effects of atmospheric turbulence and building sway on optical wireless-communication systems," *Opt. Lett.*, vol. 28, no. 2, pp. 129–131, Jan. 2003.

[81] H. G. Sandalidis, T. A. Tsiftsis, and G. K. Karagiannidis, "Optical wireless communications with heterodyne detection over turbulence channels with pointing errors," *J. Lightw. Technol.*, vol. 27, no. 20, pp. 4440–4445, Oct. 15, 2009.

[82] L. Yang, X. Gao, and M.-S. Alouini, "Performance analysis of relay-assisted all-optical FSO networks over strong atmospheric turbulence channels with pointing errors," *J. Lightw. Technol.*, vol. 32, no. 23, pp. 4011–4018, Dec. 1, 2014.

[83] M. D. Yacoub, "The α-μ distribution: A physical fading model for the stacy distribution," *IEEE Trans. Veh. Technol.*, vol. 56, no. 1, pp. 27–34, Jan. 2007.

[84] H. Lei, C. Gao, Y. Guo, and G. Pan, "On physical layer security over generalized gamma fading channels," *IEEE Commun. Lett.*, vol. 19, no. 7, pp. 1257–1260, Jul. 2015.

[85] F. Yilmaz and M.-S. Alouini, "A unified MGF-based capacity analysis of diversity combiners over generalized fading channels," *IEEE Trans. Commun.*, vol. 60, no. 3, pp. 862–875, Mar. 2012.

[86] S. G. Krantz, *Handbook of Complex Variables*. Springer, 1999.

[87] X. Pang *et al.*, "100 Gbit/s hybrid optical fiber-wireless link in the W-band (75–110 GHz)," *Opt. Express*, vol. 19, no. 25, pp. 24944–24949, Dec. 2011.

[88] A. Hirata *et al.*, "120-GHz-band millimeter-wave photonic wireless link for 10-Gb/s data transmission," *IEEE Trans. Microw. Theory Techn.*, vol. 54, no. 5, pp. 1937–1944, May 2006.

[89] A. Hirata *et al.*, "Transmission characteristics of 120-GHz-band wireless link using radio-on-fiber technologies," *J. Lightw. Technol.*, vol. 26, no. 15, pp. 2338–2344, Aug. 1, 2008.

[90] C. Han, A. O. Bicen, and I. F. Akyildiz, "Multi-wideband waveform design for distance-adaptive wireless communications in the terahertz band," *IEEE Trans. Signal Process.*, vol. 64, no. 4, pp. 910–922, Feb. 2016.

[91] A. Papoulis and S. Pillai, *Probability, Random Variables, and Stochastic Processes* (McGraw-Hill Series in Electrical Engineering: Communications and Signal Processing). New York, NY, USA: McGraw-Hill, 2002.

[92] V. S. Adamchik and O. I. Marichev, "The algorithm for calculating integrals of hypergeometric type functions and its realization in reduce system," in *Proc. Int. Symp. Symbolic Algebr. Comput. (ISSAC)*, Tokyo, Japan, Jul. 1990, pp. 212–224.

[93] *The Wolfram Functions Site*. Accessed: Aug. 8, 2018. [Online]. Available: http://functions.wolfram.com/07.34.21.0012.01

ALEXANDROS-APOSTOLOS A. BOULOGEORGOS (S'11–M'16) was born in Trikala, Greece, in 1988. He received the Electrical and Computer Engineering Diploma (ECE) degree and the Ph.D. degree in wireless communications from the Aristotle University of Thessaloniki (AUTh), in 2012 and 2016, respectively.

Since 2012, he has been a member of the Wireless Communications System Group, AUTh, where he was a Research Assistant/Project Engineer, working on various telecommunication and networks projects. From 2012 to 2016, he was a Teaching Assistant with the Department of ECE, AUTh. In 2017, he joined the Information Technologies Institute. Since 2017, he has been a member of the Department of Digital Systems, University of Piraeus, where he conducts research in the area of wireless communications. Since 2017, he has been serving as an Adjacent Lecturer with the Department of Informatics and Telecommunications Engineering, University of Western Macedonia, and as a Visiting Lecturer with the Department of Computer Science and Biomedical Informatics, University of Thessaly.

He has authored or co-authored more than 35 technical papers, which were published in scientific journals and presented at prestigious international conferences. He has submitted two (one national and one European) patents. His current research interests include the areas of wireless communications and networks with an emphasis on high-frequency communications, optical wireless communications, and communications for biomedical applications. He is a member of the Technical Chamber of Greece. He has been involved as a member of the Technical Program Committees in several IEEE and non-IEEE conferences. He received the Distinction Scholarship Award from the Research Committee of AUTh, for the year 2014. He was recognized as an Exemplary Reviewer for the IEEE COMMUNICATIONS LETTERS, in 2016 (top 3% of reviewers). He has served as a Reviewer of various IEEE journals and conferences.

EVANGELOS N. PAPASOTIRIOU was born in Athens, Greece, in 1992. He received the bachelor's degree in computer science from the Department of Computer Science and Biomedical Informatics, University of Thessaly, in 2016, and the master's degree in digital communications and networks from the Department of Digital Systems, University of Piraeus, in 2018. He is currently pursuing the Ph.D. degree in wireless communications. In 2017, he joined the Department of Digital Systems, University of Piraeus, where he conducts research in the area of wireless communications.

ANGELIKI ALEXIOU received the Diploma degree in electrical and computer engineering from the National Technical University of Athens, in 1994, and the Ph.D. degree in electrical engineering from the Imperial College of Science, Technology and Medicine, University of London, in 2000. From 1999 to 2006, she was a Member of Technical Staff with Bell Laboratories, Wireless Research, Lucent Technologies (Alcatel-Lucent), Swindon, U.K., where she was a Technical Manager, from 2006 to 2009. Since 2009, she has been a Faculty Member with the Department of Digital Systems, University of Piraeus, where she conducts research and teaches undergraduate and postgraduate courses in the areas of broadband communications and advanced wireless technologies. She is the Project Coordinator of the H2020 TERRANOVA Project (ict-terranova.eu). Her current research interests include radio interface, MIMO and high frequencies (mm-wave and THz wireless) technologies, cooperation, coordination, and efficient resource management for ultra-dense wireless networks and machine-to-machine communications, and cell-less architectures based on softwarization, virtualization, and extreme resources sharing. She is a member of the IEEE and the Technical Chamber of Greece. She was a co-recipient of the Bell Labs Presidents̓, Gold Award, in 2002, for her contributions to the Bell Labs Layered Space-Time (BLAST) Project and the Central Bell Labs Teamwork Award, in 2004, for the role model teamwork and technical achievements in the IST FITNESS Project. She is the elected Chair of the Working Group on Radio Communication Technologies of the Wireless World Research Forum.

● ● ●